Scaling laws for the longitudinal heat turbulent flux in the atmospheric surface layer

Kelly Y Huang[1], Reban Niraula[1], and Gabriel G. Katul[2]

[1]University of Houston
[2]Duke University

November 05, 2025

Abstract

The longitudinal turbulent heat flux is necessary to the description of vertical momentum and energy transport in stratified atmospheric boundary layers, yet its scaling behavior with respect to thermal stratification remains uncertain in comparison to better-studied quantities such as the vertical heat flux. Here, the scaling laws of the longitudinal heat flux and its co-spectrum in the atmosphere close to the surface as a function of wall normal distance and thermal stratification are experimentally evaluated. Measurements were conducted under varying stability regimes ranging from unstable to slightly stable at two sites. The first experiment included 5 high-temporal resolution (100 Hz) velocity and temperature sensors as well as a triaxial sonic anemometer all positioned within 2 m above a bare soil surface. The second experiment included a single triaxial sonic anemometer positioned at 5 m from a grass-covered forest clearing. The analysis first examines the Reynolds-averaged Navier–Stokes equations for the longitudinal heat flux and applies similarity theory to identify the dominant terms. This analysis is then used to inform a co-spectral budget, which is used to deduce the appropriate scaling laws at large and inertial subrange scales. The proposed theory aims to reconcile discrepancies reported across field, laboratory, and numerical studies, and highlights the importance of non-conserved scale-wise flux transfer mechanisms unique to longitudinal heat flux in turbulent flows even when the longitudinal heat flux transport term is small.

Scaling laws for the longitudinal heat turbulent flux in the atmospheric surface layer

K. Y. Huang[1], R. Niraula [1], and G. G. Katul [2]

[1]Department of Mechanical and Aerospace Engineering, University of Houston, Houston, Texas, USA
[2]Department of Civil and Environmental Engineering, Duke University, Durham, North Carolina, USA

Key Points:

- New multi-level high frequency measurements on the longitudinal heat turbulent flux near the ground are presented.
- Scaling laws based on similarity theories and directional dimensional analysis are offered.
- A co-spectral budget for the scale-wise evolution of longitudinal heat flux explains contributions from large and inertial scales.

Corresponding author: K. Y. Huang, `yhuang68@uh.edu`

Abstract

The longitudinal turbulent heat flux is necessary to the description of vertical momentum and energy transport in stratified atmospheric boundary layers, yet its scaling behavior with respect to thermal stratification remains uncertain in comparison to better-studied quantities such as the vertical heat flux. Here, the scaling laws of the longitudinal heat flux and its co-spectrum in the atmosphere close to the surface as a function of wall normal distance and thermal stratification are experimentally evaluated. Measurements were conducted under varying stability regimes ranging from unstable to slightly stable at two sites. The first experiment included 5 high-temporal resolution (100 Hz) velocity and temperature sensors as well as a triaxial sonic anemometer all positioned within 2 m above a bare soil surface. The second experiment included a single triaxial sonic anemometer positioned at 5 m from a grass-covered forest clearing. The analysis first examines the Reynolds-averaged Navier–Stokes equations for the longitudinal heat flux and applies similarity theory to identify the dominant terms. This analysis is then used to inform a co-spectral budget, which is used to deduce the appropriate scaling laws at large and inertial subrange scales. The proposed theory aims to reconcile discrepancies reported across field, laboratory, and numerical studies, and highlights the importance of non-conserved scale-wise flux transfer mechanisms unique to longitudinal heat flux in turbulent flows even when the longitudinal heat flux transport term is small.

Plain Language Summary

Swirling motion or eddies in the atmosphere near the ground constantly move heat and momentum horizontally and vertically. These exchanges, which are carried out by eddies that vary appreciably in size and energy content, shape a plethora of processes such as local weather patterns, formation of micro-bursts at airports, or how pollutants and energy spread in the environment. Studies on how eddies move heat vertically to and from the ground is now a mature field when compared to its horizontal (or longitudinal) counterpart. The work here explores theoretically and experimentally through two field experiments how horizontal heat movement by eddies behaves differently under different temperature gradients near the ground. Using new high resolution temperature and velocity data, scaling laws that describe the behavior of horizontal heat transport across different eddy sizes and heights from the ground are derived and tested. The work shows that even when the horizontal heat transport seems small on average, it plays a key role in how eddies distribute energy in the lower atmosphere.

1 Introduction

The longitudinal heat flux $\overline{u'\theta_v}$ plays a central role in momentum transfer and momentum turbulent fluxes $\overline{w'u'}$ for stratified atmospheric flows, where u', w' and θ_v' are the turbulent longitudinal velocity, turbulent vertical velocity and turbulent virtual temperature, respectively, and overline is time averaging. In fact, $\overline{u'\theta_v'}$ represents the buoyancy term that acts as a source or a sink in the turbulent momentum flux conservation equation (Garratt, 1992; Mortarini et al., 2025). In non-ideal terrain, $\overline{u'\theta_v'}$ is also needed for modeling all vertical exchanges of heat and momentum in higher-order closure schemes such as those used in climate and weather forecasting (Zeman & Lumley, 1976; J. L. Lumley, 1979; Mellor & Yamada, 1982; Large et al., 1994; Guo et al., 2015). Perhaps the lack of interest in $\overline{u'\theta_v'}$ or its co-spectrum can be traced back to the disproportionate focus on daytime convective boundary layer processes, where the longitudinal heat flux cancels out in the turbulent stress budget (Zilitinkevich et al., 1999; Canuto et al., 1994). Textbooks describing the much studied atmospheric surface layer (ASL) suggest that $\overline{u'\theta_v'} = 0$ for near-neutral and unstable atmospheric stability conditions (Kaimal & Finnigan, 1994). Yet, the relation between $\overline{u'\theta_v}$ and the vertical heat flux $\overline{w'\theta_v'}$,

$$R_h = -\frac{\overline{u'\theta_v}}{\overline{w'\theta_v'}}, \tag{1}$$

has been reported for more than 35 years now (Kader et al., 1989; Kader & Yaglom, 1990). It was empirically found that for the near-neutral atmospheric surface layer, R_h varies from 3-4. With increasing instability, R_h drops to about 0.5 as near-convective conditions are approached. For stable atmospheric stratification, much less is known about the relation between the two heat fluxes except for few studies (Caughey, 1977). That the signs of $\overline{u'\theta_v'}$ and $\overline{w'\theta_v'}$ are opposite should not be a surprise given the negative correlation between w' and u' in wall-bounded flow.

Models for $\overline{u'\theta_v'}$ benefit from understanding the processes and the scales of motion that contribute to the correlation between u' and θ_v'. In this regards, the state of knowledge for the longitudinal heat flux remains lagging other terms such as the vertical heat flux $\overline{w'\theta_v'}$ or the vertical momentum flux $\overline{w'u'}$ (Panofsky & Mares, 1968). Even in the much studied inertial subrange (ISR) where Kolmogorov scaling is anticipated (Pope, 2000), the scaling laws describing the longitudinal heat flux co-spectrum $F_{u\theta_v}(k_x)$ as a function of longitudinal wavenumber k_x are not agreed upon. When $F_{u\theta_v}(k_x)$ is expressed as k_x^{-m} in the ISR (usually identified through velocity spectra), the values of m vary appreciably. The weighty Kansas experiment report values anywhere from $m = 3$ (J. Wyngaard & Coté, 1972) to $m = 5/2$ (Kaimal et al., 1972) even when the co-spectra for momentum and vertical heat fluxes follow the anticipated $k_x^{-7/3}$. However, the experiments in Minnesota (USA) and Tsimlyansk (Russia) suggest a more conventional $m = 7/3$ (Caughey et al., 1979; Kader & Yaglom, 1991) that agrees with the vertical momentum flux co-spectrum $F_{wu}(k_x)$ (J. Lumley, 1967; G. Katul et al., 2013). Field studies exploring the $F_{wu}(k_x)$ scaling where temperature can be assumed as a passive scalar report an $m = 5/3$ for some 3 decades of k_x before transitioning in a narrow range of scales to $m = 7/3$ followed by an exponential cutoff (Antonia & Zhu, 1994). In contrast, studies in the roughness sublayer of an alpine forest (Cava & Katul, 2012) in Lavarone (Italy) spanning both unstable and mildly stable conditions report $m = 7/3$ for at least two decades of wavenumbers in the ISR. Direct numerical simulations (W. Bos et al., 2004) suggest an $m = 2$ attributing deviations from $m = 7/3$ due to a finite heat flux transfer across scales. Unlike the turbulent kinetic energy dissipation rate ε, the flux transfer associated with the longitudinal heat flux across k_x is not a 'conserved' quantity and can exhibit its own exponents. Direct numerical simulations (DNS) used to calibrate the Eddy-Damped Quasi Normal Model (EDQNM) reveal an $m = 23/9$ (W. J. Bos & Bertoglio, 2007), which is close to the early field studies reporting $m = 5/2$ (Caughey, 1977).

Here, the scaling laws of $\overline{u'\theta_v}$ and its co-spectrum in the atmosphere very close to a flat surface as a function of wall normal distance and thermal stratification are experimentally evaluated using very high temporal resolution (=100 Hz) u' and θ_v' profile measurements in the atmospheric surface layer (ASL). These measurements were conducted at the Surface Layer Turbulence and Environmental Science Test (SLTEST) facility in western Utah, USA, where the surface is a desert-like dry lake bed covered with salt. Another single-level experiment utilizing conventional sonic anemometry conducted above a grass-covered forest clearing near Durham, North Carolina is also used to assess the robustness of the findings from the SLTEST. The analysis first examines the longitudinal heat flux conservation equation and applies similarity theory and other realizability constraints to identify the dominant terms. This analysis is then used to inform a co-spectral budget, which is used to explore the scaling laws at low and high wavenumbers. A discussion regarding discrepancies reported across field, laboratory, and numerical studies is presented with the aim of illustrating the significance of non-conserved flux transfer mechanisms unique to longitudinal heat flux.

2 Theory

The theory section begins with an overview and the standard conservation equations for the longitudinal heat flux. Those equations are derived from a Reynolds-Averaged Navier-Stokes (RANS) perspective and then combined with scaling arguments to offer first-order estimates on how thermal stratification impacts production, transport, and dissipation of $\overline{u'\theta_v'}$. These scaling arguments cover conventional Monin-Obukhov similarity theory, directional-dimensional analysis, and other possibilities for weakly stable stratification. Existing and new theories for the co-spectrum are then presented using dimensional considerations (W. Bos et al., 2004; W. J. Bos & Bertoglio, 2007; Cava & Katul, 2012), a constant correlation hypothesis that was tested using field studies (Antonia & Zhu, 1994), and a co-spectral budget that links the co-spectrum of the longitudinal heat flux to the better studied co-spectra of momentum and vertical heat fluxes (G. G. Katul et al., 2013; Mortarini et al., 2025).

2.1 Definitions and General Considerations

The coordinate system employed here defines x (or x_1), y (or x_2), and z (or x_3) as the longitudinal (along mean wind direction), lateral, and vertical directions, respectively, with $z = 0$ set at the ground surface. The instantaneous velocity components along these directions are u (or u_1), v (or u_2), and w (or u_3). For a stationary and planar homogeneous flow at high Reynolds number in the absence of subsidence, the turbulent longitudinal heat flux conservation equation is (Garratt, 1992; Kaimal & Finnigan, 1994; J. C. Wyngaard, 2010):

$$\frac{\partial \overline{u'\theta_v'}}{\partial t} = 0 = \underbrace{-\overline{w'u'}\ \Gamma_\theta(z) - \overline{w'\theta_v'}\ \Gamma(z)}_{Production} - \underbrace{\frac{1}{\rho}\overline{\theta_v'\frac{\partial p'}{\partial x}}}_{Pressure-Decorrelation} - \left[\underbrace{\frac{\partial \overline{w'u'\theta_v'}}{\partial z}}_{Flux-Transport} \underbrace{- D_m \overline{u'\frac{\partial^2 \theta_v'}{\partial x_j \partial x_j}} - \nu \overline{\theta_v'\frac{\partial^2 u'}{\partial x_j \partial x_j}}}_{Molecular-Dissipation}\right], \quad (2)$$

where t is time, overline indicates averaging over coordinates of statistical homogeneity (commonly time averaging in field experiments), u' and w' are the longitudinal (along x) and vertical (along z) velocity fluctuations around their mean states $\overline{U}$ and $\overline{W} = 0$ (no subsidence), θ_v' is the virtual temperature fluctuation around its mean state $\overline{\theta_v}$, $\overline{u'\theta_v'}$ is the horizontal heat flux that can be positive or negative, $\Gamma = \partial\overline{U}/\partial z$ is the mean longitudinal velocity gradient, $\Gamma_\theta = \partial\overline{\theta_v}/\partial z$ is the mean virtual temperature gradient, ρ is the air density, p' is the pressure fluctuations referenced to a hydrostatic state, $\overline{w'u'\theta_v'}$ is the vertical transport of $\overline{u'\theta_v'}$ by turbulence, D_m is the molecular diffusion coefficient for heat in air, and ν is the kinematic viscosity of air. Hereafter, the sum of the two production terms in Equation 2 is labeled as P_m and reflects the interaction between the mean flow and turbulence generating a correlation between u' and θ_v'. For notational simplicity, it is given by

$$P_m = -\left[\overline{w'u'}\ \Gamma_\theta(z) + \overline{w'\theta_v'}\ \Gamma(z)\right]. \quad (3)$$

Due to the presence of a solid boundary, $\overline{w'u'} < 0$, $\Gamma > 0$, and instability is often defined by the sign of $\overline{w'\theta_v'}$ (unstable if positive and stable if negative) or Γ_θ (unstable if negative and stable if positive). Thus, when $\overline{w'\theta_v'} \propto -\Gamma_\theta$, the two terms in P_m act in tandem to support the generation of a correlation between u' and θ_v'.

Standard closure schemes for the pressure-decorrelation are based on a linear Rotta scheme for the so-called 'slow term' modified to include an isotropization of the production of $\overline{u'\theta_v'}$ (or P_m) for the 'fast term' (Launder et al., 1975; Pope, 2000). The application of this closure begins by expressing

$$\overline{\theta'_v \frac{\partial p'}{\partial x}} = \frac{\partial \overline{\theta'_v p'}}{\partial x} - \overline{p' \frac{\partial \theta'_v}{\partial x}}.$$

Ignoring the $\partial(.)/\partial x$ term (i.e. the pressure transport term) due to planar homogeneity, and closing the pressure-scalar interaction term using

$$\frac{1}{\rho}\overline{\theta'_v \frac{\partial p'}{\partial x}} = -\overline{p' \frac{\partial \theta'_v}{\partial x}} = C_R \frac{\overline{u'\theta'_v}}{\tau_d} - C_I P_m, \tag{4}$$

yields the sought outcome, where $C_I = 3/5$ is a constant associated with the fast isotropization of the production terms P_m and whose numerical value has been derived from Rapid Distortion Theory (Launder et al., 1975; Pope, 2000; G. G. Katul et al., 2013), $C_R = 1.8$ is the Rotta constant associated with the slow pressure-rate-of-strain part (Pope, 2000), and τ_d is a de-correlation time scale that may be related to a relaxation time (to be discussed later). This so-called LRR-IP model (after Launder, Reece, and Rodi including the isotropization of the production) has been chosen because it reproduces the mean velocity and stresses in many shear flows (Pope, 2000; Choi & Lumley, 2001; Durbin, 1993; Launder et al., 1975; Hanjalić & Launder, 2021). The isotropization of the production is assumed to directly apply on P_m in the longitudinal heat flux budget through the action of the fast component of the pressure de-correlation. Inserting this closure into the longitudinal heat flux budget to solve for $\overline{u'\theta'_v}$ yields,

$$\overline{u'\theta'_v} = \frac{\tau_d}{C_R}\left[P_m\left(1 - C_I\right) - \left(\frac{\partial \overline{w'u'\theta'_v}}{\partial z} - D_m \overline{u' \frac{\partial^2 \theta'_v}{\partial x_j \partial x_j}} - \nu \overline{\theta'_v \frac{\partial^2 u'}{\partial x_j \partial x_j}}\right)\right], \tag{5}$$

In the standard Rotta closure where $C_R = 1.8$, τ_d must be interpreted as a relaxation (instead of a de-correlation) time and is given by

$$\tau_d = \frac{1}{2}\frac{\left(\overline{u'_j u'_j}\right)}{\varepsilon} \tag{6}$$

where $\overline{u'_j u'_j}/2$ is the turbulent kinetic energy (TKE) and ε is the TKE dissipation rate. Thus, for near-neutral atmospheric stability conditions,

$$\tau_d(z) = \phi_{TKE}(0)\frac{\left(u_*^2\right)}{\left[u_*^3/(\kappa z)\right]} = \phi_{TKE}(0)\frac{\kappa z}{u_*}, \tag{7}$$

where $\kappa = 0.4$ is the von Karman constant, $\phi_{TKE}(0)$ is a coefficient that links the turbulent kinetic energy (TKE) to u_*^2 for a near-neutral ASL, and $u_* = \sqrt{-\overline{u'w'}}$ is the friction velocity. This scaling for τ_d assumes that (i) the TKE budget is reduced to a balance between production and viscous dissipation (Charuchittipan & Wilson, 2009), and (ii) the TKE follows MOST for near-neutral conditions, which it does not - given that $\overline{u'u'}/u_*^2$ is well predicted by the attached eddy hypothesis for near-neutral conditions and this prediction involves the boundary layer depth (K. Y. Huang & Katul, 2022). Nonetheless, this estimate of τ_d may be interpreted as the time it takes for turbulence to adjust to any changes in mean flow gradients (especially those associated with P_m). If the flux transport term is ignored and the high Reynolds number limit is interpreted as molecular processes are not as efficient at de-correlating u' from θ'_v when compared to the pressure de-correlation, a flux-gradient relation for the longitudinal heat flux emerges due to a balance between production P_m and pressure-decorrelation (the only remaining destruction term) given as

$$\overline{u'\theta'_v} = -\frac{1 - C_I}{C_R}\tau_d\left[\overline{w'u'}\ \Gamma_\theta(z) + \overline{w'\theta'_v}\ \Gamma(z)\right]. \tag{8}$$

For a strictly neutral limit where $\Gamma_\theta \to 0$ and $\overline{w'\theta'_v} \to 0$, Equation 8 predicts a $\overline{u'\theta'_v} = 0$ because $P_m \to 0$. Likewise, in the free convective limit where $u_*^2 \to 0$ and $\Gamma \to 0$, Equation 8 also predicts $\overline{u'\theta_v'} \rightarrow 0$. For this reason, some textbooks list $\overline{u'\theta_v'} = 0$ for near-neutral to unstable atmospheric conditions (Kaimal & Finnigan, 1994) when the flow is stationary, planar homogeneous, and high Reynolds number. These findings (i.e. $P_m \rightarrow 0$) are not fully supported by near-neutral and near-convective ASL studies. Those contradictions may be suggesting that the flux-transport term can be significant. For near-neutral conditions in the ASL, a finite $\overline{w'\theta_v'}$ is common even when when buoyancy contributions to the TKE budget are small. It is this finite $\overline{w'\theta_v'}$ that may be of disproportionate significance to the budget of $\overline{u'\theta_v'}$ that is to be explored here as well. Returning to the flux transport, this term is the only term that connects the outer layer to the near-surface heat flux in the absence of any local production of $\overline{u'\theta_v'}$. To estimate the possible role of the flux transport term - at least in a first-order analysis, a gradient-diffusion closure is used and yields

$$\overline{w'u'\theta_v'} = -K_t(z)\frac{\partial \overline{u'\theta_v'}}{\partial z}. \tag{9}$$

That is, restricting the balance between flux transport and pressure-de-correlation yields an approximated longitudinal heat flux budget given by

$$K_t\frac{\partial^2 \overline{u'\theta_v'}}{\partial z \partial z} + \frac{\partial K_t}{\partial z}\frac{\partial \overline{u'\theta_v'}}{\partial z} - \frac{C_R}{\tau_d}\overline{u'\theta_v'} = 0. \tag{10}$$

In the near-neutral limit, it may be argued that $K_t = \kappa z u_*$, $\tau_d = \phi_{TKE}(0)\kappa z/u_*$, the budget in Equation 10 becomes

$$z^2\frac{\partial^2 \overline{u'\theta_v'}}{\partial z \partial z} + z\frac{\partial \overline{u'\theta_v'}}{\partial z} - a_n\,\overline{u'\theta_v'} = 0;\ a_n = \frac{C_R}{\kappa^2 \phi_{TKE}(0)^2}. \tag{11}$$

This homogeneous second-order ordinary differential equation is of the Cauchy-Euler form whose general solution is given as

$$\overline{u'\theta_v'} = B_1 z^{a_n} + B_2 z^{-a_n}. \tag{12}$$

In the limiting cases where $z \rightarrow 0$, $B_2 = 0$ and when $z \rightarrow \infty$, $B_1 = 0$. That is, the super-position of these two solutions is simply a statement of how 'bottom-up diffusion' and 'top-down' diffusion of longitudinal heat flux behave in z. For the free convective limit, K_t and τ_d are independent of z (as they vary with the convective boundary layer height) and the budget reduces to

$$\frac{\partial^2 \overline{u'\theta_v'}}{\partial z \partial z} = a_c \overline{u'\theta_v'};\quad a_c = \frac{C_R}{K_t \tau_d}. \tag{13}$$

The solution is

$$\overline{u'\theta_v'} = C_1 \exp(\sqrt{a_c} z) + C_2 \exp(-\sqrt{a_c} z). \tag{14}$$

In the limiting cases where $z \rightarrow \infty$, $C_1 = 0$ suggesting that the longitudinal heat flux decays exponentially with increasing z.

These budget considerations suggest that when variations in $\overline{u'\theta_v'}$ with z occur, the flux transport term is likely to be significant and its magnitude is commensurate with the pressure-decorrelation contribution. Conversely, when the z-dependency of $\overline{u'\theta_v'}$ is weak or insignificant, it may be argued that the flux-transport term is small and can be ignored.

2.2 Dimensional Analysis Applied to the Horizontal Heat Flux

2.2.1 A Monin-Obukhov Similarity Theory (MOST) Scaling

It may be instructive to ask what are the scaling laws for $\overline{u'\theta_v'}$ with atmospheric stability in the diabatic atmospheric surface layer (ASL) assuming Monin and Obukhov

(Monin & Obukhov, 1954) Similarity theory (MOST) holds for momentum and vertical heat transport. To connect MOST to Equation 8, the following definitions are introduced:

$$\Gamma \frac{\kappa z}{u_*} = \phi_m(\xi),\ \Gamma_\theta \frac{\kappa z}{T_*} = \phi_h(\xi),\ Pr_t = \frac{\phi_h(\xi)}{\phi_m(\xi)}, \tag{15}$$

where $T_* = -\overline{w'\theta_v'}/u_*$ is a temperature scale, $\xi = z/L_o$ is the atmospheric stability parameter, L_o is the Obukhov length given by

$$L_o = -\frac{u_*^3}{\kappa \beta \overline{w'\theta_v'}},$$

$\beta = g/\overline{\theta_v}$ is the buoyancy parameter, g is the gravitational acceleration, $\phi_m(\xi)$ and $\phi_h(\xi)$ are the stability correction functions for momentum and heat, respectively, and Pr_t is the turbulent Prandtl number with values between 0.7 to 1.0 in the near-neutral limit (Kays, 1994; Li, 2019). Inserting these MOST results into Equation 8 yields

$$\overline{u'\theta_v'} = \left(\frac{1-C_I}{C_R}\right)\left[\tau_d\ \phi_m(\zeta)\right] \frac{u_*^2 T_*}{\kappa z}\left[1 + Pr_t(\xi)\right]; \tau_d = \frac{\kappa z}{u_*}\left[\frac{\phi_{TKE}(\xi)}{\phi_\varepsilon(\xi)}\right], \tag{16}$$

where $\phi_\varepsilon(\xi)$ is the stability correction function for ε presented elsewhere (Hsieh & Katul, 1997). Because a number of studies report the relative importance of horizontal to vertical heat flux or R_h (Kader & Yaglom, 1990), Equation 16 is re-casted as

$$R_h = -\frac{\overline{u'\theta_v'}}{\overline{w'\theta_v'}} = \left(\frac{1-C_I}{C_R}\right)\left[\tau_d\ \phi_m(\xi)\right] \frac{u_*}{\kappa z}\left[1 + Pr_t(\xi)\right]. \tag{17}$$

Inserting Equation 6 into Equation 17 yields an R_h estimate based on dimensionless stability correction functions given by

$$R_h = -\frac{\overline{u'\theta_v'}}{\overline{w'\theta_v'}} = \left(\frac{1-C_I}{C_R}\right)\left[\frac{\phi_{TKE}(\xi)\ \phi_m(\xi)}{\phi_\varepsilon(\xi)}\right]\left[1 + \frac{\phi_h(\xi)}{\phi_m(\xi)}\right]. \tag{18}$$

For small $|\xi|$ (i.e. near-neutral), setting $Pr_t(0) = 1$, and noting that $C_R = 1.8$, $C_I = 3/5$, $\phi_m(0) = 1$, $\phi_\varepsilon(0) = 1$, $\phi_{TKE}(0) = 6.7$ yields

$$R_h = -\frac{\overline{u'\theta_v'}}{\overline{w'\theta_v'}} = 3.$$

This estimate, which did not involve any 'tunable' parameters, is close to the family of ASL experiments (Kader & Yaglom, 1990) reporting values between 3.5-4.0 for near-neutral conditions (especially their Figures 3 and 4). This agreement lends some confidence in the closure scheme employed when sensible heat flux is small but finite (i.e. does not contribute appreciably to the TKE budget) yet the flow remains near-neutral due to a high u_*.

2.2.2 Realizability Constraint on the Longitudinal Heat Flux

That R_h is larger than unity in magnitude may have been foreshadowed when noting that

$$R_h = -\frac{\overline{u'\theta_v'}}{\overline{w'\theta_v'}} = -\frac{R_{u\theta}}{R_{w\theta}}\frac{\sigma_u}{\sigma_w},$$

where $R_{ab} = \overline{a'b'}/(\sigma_a\sigma_b)$ is the correlation coefficient between two variables (a and b). Since attached eddies or eddies associated with a k_x^{-1} scaling exponent in the spectra of u' and θ_v' for near-neutral conditions (Kader & Yaglom, 1991; G. G. Katul et al., 1995; K. Y. Huang & Katul, 2022; K. Y. Huang et al., 2023) contribute to $R_{u\theta_v}$ but less so to $R_{w\theta}$ (the spectrum of w' is flat for $k_x z < 1$), it is anticipated that $|R_{u\theta_v}/R_{w\theta_v}| > 1$.

Moreover, $\sigma_u/\sigma_w > 2$ due to the presence of the wall. These considerations alone lead to $|R_h| > 2$.

A further refinement may be achieved from a statistical point of view by considering the correlation coefficients between three arbitrary normalized variables selected here to be u'/σ_u, w'/σ_w, and θ_v'/σ_θ. These three normalized variables can be used to form a symmetric and thus positive-definite matrix A_c. Because it is positive definite, its determinant must be positive and is given by (Bink & Meesters, 1997; G. Katul & Hsieh, 1997; Priestley, 1988)

$$\det(A_c) = \det \begin{bmatrix} 1 & R_{u\theta} & R_{w\theta} \\ R_{u\theta} & 1 & R_{uw} \\ R_{w\theta} & R_{uw} & 1 \end{bmatrix} = 1 + 2R_{uw}R_{u\theta}R_{w\theta} - (R_{u\theta}^2 + R_{w\theta}^2 + R_{uw}^2) \geq 0.$$

This condition, which holds for any symmetric matrix with real-valued finite elements, can now be employed to set an upper bound on $R_{u\theta}$ using the more studied $R_{w\theta}$ and R_{uw}. That is,

$$R_{u\theta} \in R_{uw}R_{w\theta} \pm \sqrt{1 + R_{uw}^2 R_{w\theta}^2 - (R_{uw}^2 + R_{w\theta}^2)}, \quad (19)$$

or

$$|R_{u\theta}| \leq |R_{uw}R_{w\theta}| + \sqrt{1 + R_{uw}^2 R_{w\theta}^2 - (R_{uw}^2 + R_{w\theta}^2)}. \quad (20)$$

For near-neutral to slightly unstable conditions, $R_{w\theta} = 0.5$, $R_{uw} = -0.35$ (Kaimal & Finnigan, 1994), thereby bounding $R_{u\theta} \in [-0.99, +0.64]$. With this statistical bound, $R_h = -(-0.99/0.5) \times (2.7/1.25) = 4.4$, which is expected to be higher than the prediction of $R_h = 3$ using the closure scheme from Equation 18 and near-neutral limits. Yet, $R_h = 4.4$ is below the experimental value $R_{u\theta} = 4$ reported from long-term field studies for near-neutral conditions (Kader & Yaglom, 1990). These findings offer a plausibility check that the R_h model in Equation 18 with $C_R = 1.8$, $C_I = 3/5$, and $\phi_{TKE}(0) = 6.7$ is compatible with estimates using other independent flow quantities in the ASL ($R_{w\theta} = 0.5$, $R_{uw} = -0.35$).

2.2.3 A Directional Dimensional Analysis (DDA) for Unstably Stratified Flows

The DDA, pioneered for the ASL in the early 1970s (Betchov & Yaglom, 1971; Zilitinkevich, 1973), was formalized and expanded for unstable conditions in the early 1990s (Kader & Yaglom, 1990). The DDA begins by noting that the generation of TKE occurs from two sources when the atmosphere is unstable: mechanical production ($P_{uu} = -\overline{w'u'}\Gamma$) from $\overline{u'u'}$ injected in the horizontal and buoyancy production ($P_{ww} = \beta\overline{w'\theta_v'}$) from $\overline{w'w'}$ injected in the vertical. DDA also assumes that these two TKE generation mechanisms are, to a leading order, decoupled. It then associates separate horizontal and vertical length scales (L_x and L_z) to each (directional) generation mechanism. Length scales associated with generating u' (through P_{uu}) are characterized by L_x whereas processes generating w' (through P_{ww}) are associated with L_z. A drawback of this approach is that it ignores interactions between these two components that may occur due to pressure redistribution and return to isotropy (Bou-Zeid et al., 2018). Nonetheless, when the generation mechanisms of u' and w' occur at scales much larger than the scales at which return to isotropy becomes effective, the assumptions behind DDA may still hold. Some indirect support for this conjecture was recently reported using ASL experiments in the context of scale-wise return to isotropy of the stress tensor from production to inertial for a large number of atmospheric conditions (Brugger et al., 2018; Stiperski et al., 2021). The DDA further assumes that a single characteristic time t_c (no directional association) exists. Accepting the 'decoupling' between L_x and L_z implies that $u_*^2 = -\overline{u'w'}$ is associated with $L_x L_z t_c^{-2}$. Thus, u_* does not 'qualify' as a horizontal velocity scale when ground heating or cooling occurs. DDA further argues that a local characteristic vertical velocity having dimensions L_z/t_c, but encoding buoyancy sources, can also be defined using $w_* = \left(\beta\overline{w'T'}z\right)^{1/3}$ for the ASL. With these arguments, DDA proposes a new

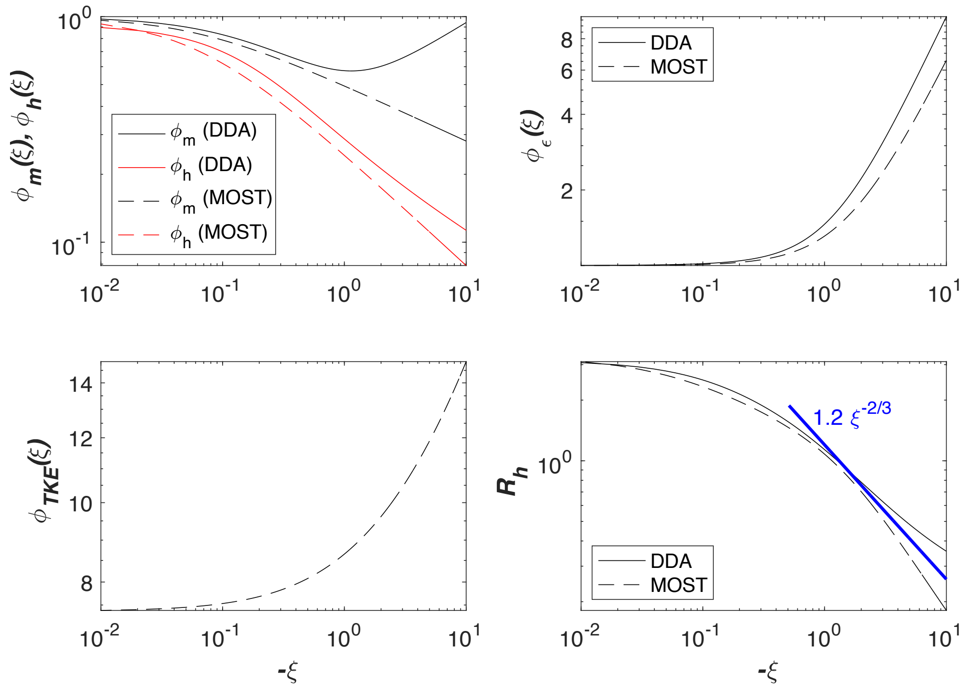

Figure 1. Comparison between DDA and MOST predictions of R_h using the budget in Equation 18. Top-left: Comparisons between DDA and MOST stability correction functions for ϕ_m and ϕ_h, Top-right: Comparison between DDA and MOST stability correction functions for ϕ_ε, Bottom-left: ϕ_{TKE} assuming only σ_w/u_* varies with ξ whereas σ_u/u_*=2.7 and σ_v/u_*=2.3 are held constant in the dynamic and dynamic-convective range. Bottom-right: Predicted $R_h = -\overline{u'\theta'_v}/\overline{w'\theta'_v}$ for DDA (solid) and MOST (dashed) stability correction functions.

horizontal velocity that must be formed from L_x/t_c and a logical choice would be a $u_{**} = u_*^2/w_*$. Likewise, the ASL temperature scale T_* must be replaced by $T_{**} = \overline{w'T'}/w_*$. The ensuing analysis proposes that the ASL be decomposed into 3 sub-layers: dynamic (or near-neutral and already discussed), dynamic-convective and free convective (Kader & Yaglom, 1990). Hence, for the dynamic convective case, DDA argues that

$$\frac{\overline{u'\theta'_v}}{u_{**}T_{**}} = \frac{w_*^2}{u_*^2}\frac{\overline{u'\theta'_v}}{\overline{w'\theta'_v}} = \text{constant}.$$

Thus, DDA predicts that

$$R_h = -\frac{\overline{u'\theta'_v}}{\overline{w'\theta'_v}} = \text{constant } \times \frac{u_*^2}{w_*^2} = \text{constant } \times \frac{u_*^2}{\left(\beta\overline{w'T'}z\right)^{2/3}} = \text{constant } \times \kappa^{2/3}\xi^{-2/3}.$$

This DDA prediction was confirmed using multiple data sources (Kader & Yaglom, 1990). A comparison between predicted R_h from Equation 18 using MOST and DDA stability correction functions is shown in Figure 1.

2.2.4 A Dougherty-Ozmidov Scaling for Stably Stratified Flows

For near neutral to slightly stable conditions, it may be argued that MOST applies and the usual corrections can be used in the longitudinal heat flux budgets. However, as the effects of stable stratification increase (e.g. $|\xi| > 0.2$), L_o is no longer the most appropriate length scale characterizing the effects of stratification on eddy sizes. Instead, the Dougherty-Ozmidov scale L_{DO} may be the relevant length because it is the size of the largest eddy unaffected by buoyancy (Dougherty, 1961; Grachev et al., 2015; Li et al., 2016). Thus, when $z/L_{DO} \ll 1$, MOST scaling applies. However, when $z/L_{DO} > 1$, the Dougherty-Ozmidov scaling variables may be more relevant. The appropriate length, velocity, and temperature normalizing variables associated with the Doughtery-Ozmidov scaling are (Li et al., 2016; Grachev et al., 2015):

$$L_{DO} = \left(\frac{\varepsilon}{N_{BV}^3}\right)^{1/2}; U_{DO} = \left(\frac{\varepsilon}{N_{BV}}\right)^{1/2}; \theta_{DO} = \frac{\sqrt{\varepsilon N_{BV}}}{\beta}; N_{BV} = \sqrt{\beta \Gamma_\theta},$$

where N_{BV} is the Brunt-Vaisala frequency. Thus, it may be anticipated that for stable stratification,

$$\frac{\overline{u'\theta_v'}}{U_{DO}\ \theta_{DO}} = \phi_{u\theta}(\xi).$$

2.3 The Longitudinal Heat Flux Co-Spectrum

Moving from RANS analysis to co-spectral analysis, the shape of the longitudinal heat flux co-spectrum $F_{u\theta_v}(k_x)$ with k_x is now considered. The co-spectrum satisfies the normalizing property

$$\frac{\int_0^\infty F_{u\theta_v}(k_x) dk_x}{\overline{u'\theta_v'}} = 1. \quad (21)$$

2.3.1 Dimensional Analysis for the Inertial Subrange: A Review

For the ISR, the possible list of variables to be included are as follows (Tennekes & Lumley, 1972):

- Eddy sizes or wavenumbers: k_x,
- Standard ISR variables in 'conservative' cascades that include ε and temperature variance dissipation rate ε_θ. They are relevant when the transfer of TKE and $\overline{\theta_v'^2}$ across scales or k_x are dissipated by molecular processes (i.e. kinematic viscosity and thermal diffusivity),
- External mean flow effects that act on all k_x in the generation mechanism: $\Gamma = \partial\overline{U}/\partial z$ and $\Gamma_\theta = \partial\overline{\theta_v}/\partial z$.

With this list and upon defining length [L], time [T], and temperature [K] as basic dimensions, it is straightforward to show that (Mortarini et al., 2025)

$$F_{u\theta_v}(k_x) = k_x^a \varepsilon^b \varepsilon_\theta^c \Gamma^d \Gamma_\theta^e; \quad \frac{[L]^2[K]}{T} = \left(\frac{1}{[L]}\right)^a \left(\frac{L^2}{[T]^3}\right)^b \left(\frac{[K]^2}{[T]}\right)^c \left(\frac{1}{[T]}\right)^d \left(\frac{[K]}{[L]}\right)^e, \quad (22)$$

leading to the following dimensional constraints:

$$[K] : 1 = 2c + e \quad (23)$$
$$[T] : 1 = 3b + c + d \quad (24)$$
$$[L] : 2 = -a + 2b - c. \quad (25)$$

That is, five variables and 3 dimensions are available and the problem is indeterminate. However, limiting cases can still be derived and are summarized below:

- When $F_{u\theta_v}(k_x)$ is assumed to vary with k_x, ε and ε_θ (i.e. no mean gradients or production variables), dimensional analysis requires that $F_{u\theta_v}(k_x) \sim \varepsilon_\theta^{1/2}\varepsilon^{1/6}k_x^{-5/3}$. This scaling is compatible with the constant correlation coefficient later described.
- When $F_{u\theta_v}(k_x)$ is assumed to vary with k_x and mean gradient quantities only (i.e. Γ, and Γ_θ - and thus dominated by production terms), then $F_{u\theta_v}(k_x) \sim (\Gamma)(\Gamma_\theta)k_x^{-3}$.

- When $F_{u\theta_v}(k_x)$ is assumed to vary with k_x, ε_θ and Γ (i.e. mixed quantities), then $F_{u\theta_v}(k_x) \sim (\Gamma\varepsilon_\theta)^{1/2}k_x^{-2}$.
- When $F_{u\theta_v}(k_x)$ is assumed to vary with $k_x^{-5/2}$ (reported in several studies), ε_θ, Γ, and Γ_θ, then $F_{u\theta_v}(k_x) \sim (\Gamma\varepsilon_\theta)^{1/2}\Gamma_\theta^{-1}k_x^{-5/2}$.
- When $F_{u\theta_v}(k_x)$ is assumed to vary with k_x, ε and Γ_θ (another mixed quantity), then $F_{u\theta_v}(k_x) \sim \Gamma_\theta\varepsilon^{1/3}k_x^{-7/3}$.

These results cover the entire range of scaling exponents already reported in the literature for the ISR. When combined with the analysis of the RANS budget, the following conjectures can be made: In the asymptotic near-convective and near-neutral limits, the terms associated with P_m are not significant and $k_x^{-5/3}$ is expected to hold for the ISR. For the dynamic convective limit, where Γ and Γ_θ are large, mixed scaling is likely to dominate (i.e. $k_x^{-6/3}$ to $k_x^{-7/3}$). For mildly stable conditions, a $k_x^{-7/3}$ was also confirmed (Caughey, 1977).

One more prediction in the ISR was offered from the Eddy-Damped Quasi Normal Model (EDQNM). In this analysis, ε_θ was excluded and it directly follows from the reduced dimensional considerations here (i.e. $c = 0$) that the co-spectrum is given by (W. J. Bos & Bertoglio, 2007)

$$F_{u\theta_v}(k_x) \sim \Gamma_\theta\Gamma^d\varepsilon^{(1-d)/3}k_x^{-(7+2d)/3}, \tag{26}$$

where $d = 1/3$ was determined using DNS. With such a d, Equation 26 becomes

$$F_{u\theta_v}(k_x) \sim \Gamma_\theta\Gamma^{1/3}\varepsilon^{2/9}k_x^{-23/9}. \tag{27}$$

The exponent $23/9 = 2.55$ is close to what was reported for some field experiments (Kaimal et al., 1972) where an exponent $= 5/2$ was empirically determined.

2.3.2 Dimensional Analysis for Large Eddies

For a near-neutral limit and upon assuming L_p characterizes large scale eddies, a plausible choice for the normalizing variables of the co-spectrum are L_p, u_*, and T_* so that

$$\frac{F_{u\theta_v}(k_x)}{u_*T_*L_p^{-1}} = f(k_xL_p). \tag{28}$$

There are two choices for L_p: an inner-layer (i.e. $L_p = z$) scaling and an outer-layer ($L_p = \delta$, where δ is the boundary layer depth) scaling. For scales much larger z but much smaller than δ, it is anticipated that both z and δ are no longer relevant length scales. Thus, L_p cannot be a dynamically relevant variable in this intermediate region. To eliminate L_p, $f(k_xL_p) = C_1(k_xL_p)^{-1}$, which yields

$$F_{u\theta_v}(k_x) = C_1u_*T_*k_x^{-1} = C_1\left(\overline{w'\theta_v'}\right)k_x^{-1}. \tag{29}$$

The k_x^{-1} scaling has received experimental support (Kader & Yaglom, 1991) for the dynamic sublayer and the free convective limit with $C_1 = -0.6$ for the dynamic sublayer and $C_1 = -0.14$ for the free convective limit. The same study did not report the $F_{u\theta_v}(k_x)$ stating that the situation is more complicated for this term.

In mildly stable stratification, it was reported that $F_{u\theta_v}(k_x)$ scales as k_x^{-1} up to low frequencies commensurate to $N_{BV} = \sqrt{\beta\Gamma_\theta}$ but for much smaller eddy sizes, $F_{u\theta_v}(k_x)$ scales as $k_x^{-5/2}$ (Caughey, 1977). The k_x^{-1} scaling for large eddies and mildly stable conditions can also be derived from normalizing by the Doughtery-Ozmidov variables assuming a power-law co-spectrum to yield

$$\frac{F_{u\theta_v}(k_x)}{(U_{DO})(\theta_{DO})(L_{DO}^{-1})} = \left[\frac{\beta}{\varepsilon^{1/2}N_{BV}^{3/2}}\right]F_{u\theta_v}(k_x) = (k_xL_{DO})^{-a}; \tag{30}$$

To eliminate ε, which is used as a normalizing variable for fine-scales, $a = 1$ and

$$F_{u\theta_v}(k_x) = \frac{1}{\beta} N_{BV}^3 k_x^{-1} \tag{31}$$

Interestingly, for frequencies much smaller than N_{BV}, an approximate k_x^{-3} scaling was also reported for the aforementioned study. This scaling is consistent with Γ and Γ_θ being the only dynamically relevant variables describing very large scales (i.e. those commensurate with mean-flow variables).

2.3.3 The Constant Scalewise Correlation Hypothesis

One field study reports a constant scale-wise correlation coefficient defined as (Antonia & Zhu, 1994)

$$\frac{F_{u\theta}(k_x)}{F_{uu}(k_x)^{1/2} F_{\theta\theta}(k_x)^{1/2}} = \text{constant}. \tag{32}$$

This constant correlation appeared to extend to scales larger than those associated with the ISR. For ISR scales, setting $F_{uu}(k_x) = C_o \varepsilon^{2/3} k_x^{-5/3}$ and $F_{\theta\theta}(k_x) = C_T \varepsilon_\theta \varepsilon^{-1/3} k_x^{-5/3}$, the constant correlation coefficient argument would lead to

$$F_{u\theta}(k_x) = \sqrt{C_T C_o} \varepsilon^{1/6} \varepsilon_\theta^{1/2} k_x^{-5/3}, \tag{33}$$

where $C_o = 0.55$ is the Kolmogorov constant and $C_T = 0.8$ is the Kolmogorov-Obukhov-Corrsin constant (Kaimal & Finnigan, 1994; Hsieh & Katul, 1997).

This is the expected outcome when Γ and Γ_θ are not introduced as dynamically relevant, which is equivalent to assuming that the generation mechanism is weak and only energy transfer across scales is relevant. To what degree this constant-correlation hypothesis holds across stability regimes, heights from the grounds, and scales larger than the ISR have not been fully explored and motivate the analysis here.

2.3.4 A Co-Spectral Budget (CSB): General Considerations

A scale-by-scale budget for $F_{u\theta}(k_x)$, hereafter referred to as the co-spectral budget (CSB), mirroring the terms in the stationary RANS model may be written as

$$\frac{\partial}{\partial t} F_{u\theta}(k_x) = 0 = P_{u\theta}(k_x) + T_{u\theta}(k_x) + \pi_{u\theta}(k_x) - (\nu + D_m) k_x^2 F_{u\theta}(k_x), \tag{34}$$

where $P_{u\theta}(k_x)$ is the scale-wise production (mirroring P_m), $T_{u\theta}(k_x)$ is the scale-wise heat flux transfer (mirroring the flux transport), $\pi_{u\theta}(k_x)$ is the pressure de-correlation term, and the last term are the molecular terms decorrelating u' from θ_v' at scale k_x. Those molecular terms are expected to be significant at scales commensurate to the Kolmogorov micro-scales. The $P_{u\theta}(k_x)$ is given by

$$P_{u\theta}(k_x) = F_{wu}(k_x)\ \Gamma_\theta(z) + F_{w\theta}(k_x)\ \Gamma(z), \tag{35}$$

where $F_{uw}(k_x)$ and $F_{w\theta}(k_x)$ are the momentum and sensible heat flux co-spectra, respectively. The pressure de-correlation may be modeled using a spectral Rotta scheme given as (Besnard et al., 1996; G. G. Katul et al., 2014; Li, 2019)

$$\pi_{u\theta}(k_x) = -\frac{C_R}{\tau_d(k_x)} F_{u\theta}(k_x) - C_I P_{u\theta}(k_x), \tag{36}$$

where $\tau_d(k_x)$ is a scale-dependent relaxation time presumed to vary with ε and k_x. For the inertial subrange, $\tau_d(k_x) = \varepsilon^{-1/3} k_x^{-2/3}$ but for eddy sizes much larger than their inertial subrange counterparts, $\tau_d(k_x) = \varepsilon^{-1/3} k_a^{-2/3}$, where k_a is an inverse of a macro-scale eddy size (e.g. $\sim 1/L_p$). Much like the flux transport term in RANS, the flux transfer term across scales also requires a spectral closure model. A typical closure scheme assumes that the longitudinal heat flux occurs 'down-scale' by diffusion and is given by

$$T_{u\theta}(k_x) = -\frac{\partial}{\partial k_x}\left[\frac{A_{u\theta} k_x}{\tau_d(k_x)}\right] F_{u\theta}(k_x), \tag{37}$$

where $A_{u\theta}$ is a similarity coefficient. This closure model assumes that the scale-wise flux transfer is only driven by local interactions and any non-local transfer must be either small or is accommodated by a non-universal A_u. Using this spectral closure scheme, the overall flux transport term in RANS, represented by the scale-wise integrated flux transfer term here, remains negligible because

$$\int_0^\infty T_{u\theta}(k_x) dk_x = -A_{u\theta}\left[\frac{k_x}{\tau_d(k_x)} F_{u\theta}(k_x)\right]_{k_x=0}^{k_x=\infty} = 0. \tag{38}$$

Equation 38 is satisfied when $F_{u\theta}(k_x) \to 0$ faster than $[k_x/\tau_d(k_x)] \to \infty$ as $k_x \to \infty$. This condition is ensured because ignoring the molecular destruction terms necessitates that $k_x^2 F_{u\theta} \to 0$ as $k_x \to \infty$. To summarize, $T_{u\theta}(k_x)$ need not be zero at every k_x even when the flux transport term is ignored in a RANS analysis.

A locally equilibrated CSB whereby the scale-by-scale balance is between production and pressure-redistribution yields

$$F_{u\theta_v}(k_x) = -\frac{1 - C_I}{C_R} \tau_d(k_x) \left[F_{wu}(k_x)\ \Gamma_\theta(z) + F_{w\theta}(k_x)\ \Gamma(z)\right]. \tag{39}$$

In this case, the molecular terms are ignored and $A_{u\theta}$=0. In what follows, the CSB is discussed separately for large-scales and inertial subrange scales given the different representation for $\tau_d(k_x)$ in these two regimes.

2.3.5 The CSB in the Inertial Subrange

When the transfer and molecular terms are ignored thereby reducing the CSB to a balance between $P_{u\theta}(k_x)$ and $\pi_{u\theta}(k_x)$, Equation 39 predicts that $F_{u\theta_v}(k_x)$ scales as $k_x^{-7/3}$ when both $F_{uw}(k_x)$ and $F_{w\theta}(k_x)$ scale as $k_x^{-7/3}$. However, retaining the transfer term, ignoring the molecular terms, and setting $\tau_d = \varepsilon^{-1/3} k_x^{-2/3}$ results in

$$\frac{\partial F_{u\theta}(k_x)}{\partial k_x} + \left[\frac{5}{3} + \frac{C_R}{A_{u\theta}}\right] \frac{F_{u\theta}(k_x)}{k_x} = \left(\frac{1 - C_I}{A_{u\theta}\ \varepsilon^{1/3}}\right) \left[F_{uw}(k_x)\Gamma_\theta + F_{w\theta}(k_x)\Gamma\right] k_x^{-5/3}. \tag{40}$$

As with the RANS model, it is instructive to ask what is the limiting behavior of $F_{u\theta}(k_x)$ when $P_{u\theta}(k_x) \to 0$. Mathematically, this limit sets the homogeneous solution of Equation 40, while $P_{u\theta}(k_x)$ dictates the particular solution. The sum of these two solutions, homogeneous and particular, set the general solution for the co-spectral budget model in the inertial subrange. The homogeneous solution is given by

$$F_{u\theta}(k_x) = C_h k_x^{-5/3-(C_R/A_{u\theta})}, \tag{41}$$

where C_h is an integration constant that is related to a finite $\overline{u'\theta_v'}$ introduced at some scale that is then transferred to finer scales and dissipated by the pressure de-correlation term. The homogeneous solution is suggestive that deviations from a $F_{u\theta}(k_x) \sim k_x^{-5/3}$ scaling is linked to a finite $A_{u\theta}$. With a $C_R = 1.8$ and an $A_{u\theta} = 2.7$, the $F_{u\theta}(k_x) \sim k_x^{-7/3}$ is recovered. Likewise, an $F_{u\theta}(k_x) \sim k_x^{-5/2}$ and an $F_{u\theta}(k_x) \sim k_x^{-23/9}$ are recovered when setting, respectively, $A_{u\theta} = 2.16$ and $A_{u\theta} = 2.025$. Thus, a non-universal exponent for $F_{u\theta}(k_x)$ in the ISR may depend on the significance of the flux-transfer term. To solve Equation 40, $F_{uw}(k_x)$ and $F_{w\theta}(k_x)$ must be known or externally supplied. Upon imposing canonical shapes for these two co-spectra as derived from a reference height in the ASL well above the ground, contributions of the $P_{u\theta}(k_x)$ on the longitudinal heat flux co-spectrum can be explored directly using Equation 39 and indirectly using Equation 40. It is to be noted that when $P_{u\theta}(k_x) = A_p k_x^{-\beta_p}$ (i.e. a power-law), the general solution may be expressed as

$$F_{u\theta}(k_x) = \underbrace{C_h k_x^{-5/3-(C_R/A_{u\theta})}}_{Homogeneous} + \underbrace{\left(\frac{1-C_I}{A_{u\theta}\varepsilon^{1/3}}\right)\frac{A_p}{1-\beta_p+(C_R/A_{u\theta})}k_x^{-2/3-\beta_p}}_{Particular}. \quad (42)$$

Distortions from the $P_{u\theta}(k_x)$ to the inertial subrange of $F_{u\theta}(k_x)$ can thus be traced through the value of β_p across different stability regimes. Also dynamically interesting is the value of $A_{u\theta}$. As $A_{u\theta}$ increases and becomes much larger than $C_R(=1.8)$, the $F_{u\theta}(k_x)$ becomes dominated by the homogeneous solution that trends towards $k_x^{-5/3}$. Conversely, when $A_{u\theta}$ decreases, the homogeneous solution decays with increasing k_x rapidly and the particular solution (i.e. $-2/3-\beta_p$) dominates the scaling exponent of $F_{u\theta}(k_x)$. Thus, the scaling laws describing $F_{u\theta}(k_x)$ depend on two quantities that need not be universal: $A_{u\theta}$ (arising from the flux transfer contribution) and β_p (arising from the production contribution to the inertial subrange). This finding alone may explain why no consistent inertial subrange exponent was reported in the literature for $F_{u\theta}(k_x)$.

2.3.6 The CSB for the Large Scales

As before, retaining the transfer term, ignoring the molecular terms, and setting $\tau_d = \varepsilon^{-1/3}k_a^{-2/3}$ results in a revised model given by

$$\frac{\partial F_{u\theta}(k_x)}{\partial k_x} + \left[1+\frac{C_R}{A_{u\theta}}\right]\frac{F_{u\theta}(k_x)}{k_x} = \left(\frac{1-C_I}{A_{u\theta}\ \varepsilon^{1/3}k_a^{2/3}}\right)\left[F_{uw}(k_x)\Gamma_\theta + F_{w\theta}(k_x)\Gamma\right]k_x^{-1}. \quad (43)$$

Upon setting $P_{u\theta}(k_x) = A'_p k_x^{-\beta'_p}$ (coefficients can differ from their inertial subrange), the general solution is

$$F_{u\theta}(k_x) = \underbrace{C_h k_x^{-1-(C_R/A_{u\theta})}}_{Homogeneous} + \underbrace{\left(\frac{1-C_I}{A_{u\theta}\varepsilon^{1/3}k_a^{2/3}}\right)\frac{A'_p}{1+(C_R/A_{u\theta})}k_x^{-\beta'_p}}_{Particular}. \quad (44)$$

Once again, as $A_{u\theta}$ increases and becomes much larger than $C_R(=1.8)$, the $F_{u\theta}(k_x)$ becomes dominated by the homogeneous solution that trends towards k_x^{-1}. Conversely, when $A_{u\theta}$ decreases, the homogeneous solution decays with increasing k_x rapidly and the particular solution (i.e. $-\beta'_p$) dominates the scaling exponent of $F_{u\theta}(k_x)$. Thus, the scaling laws describing $F_{u\theta}(k_x)$ at large scales also depend on the same two quantities that need not be universal: $A_{u\theta}$ (arising from the flux transfer contribution) and β'_p (arising from the production contribution at large scales).

3 Experiments

Two ASL experiments described elsewhere (G. Katul et al., 1997; K. Huang et al., 2021; K. Y. Huang et al., 2023) were used to assess the findings of the models. The main experiment involved a vertical array of 5 probes measuring (u') and temperature sensors near the ground (0.06-1 m) supplemented by a triaxial sonic anemometer measuring u', v', w' and θ'_v at z=2 m over a uniform and flat site. The second experiment involved a single triaxial sonic anemometer positioned at z=5.2 m above a large grass-covered forest clearing. This experiment is used to assess the robustness of the findings derived from the main experiment. Figure 2 shows the differences in surface cover and surroundings at these two sites.

3.1 SLTEST

The main experiment was conducted at the Surface Layer Turbulence and Environmental Science Test (SLTEST) facility in western Utah, USA, during the Idealized horizontal Planar Array experiment for Quantifying Surface heterogeneity (IPAQS) in June 2018. Located in the Great Salt Lake Desert, the SLTEST site is characterized by low surface roughness (with long uninterrupted fetches in the dominant wind direction) and strong thermal heterogeneity (owing to salt patches on the surface created by variations in soil and salt deposits).

Measurements from a triaxial sonic anemometer and a nearby vertical array of miniature hot- and cold-wires located ≈10 m east of the triaxial sonic anemometer were used. The sonic anemometer (Campbell Scientific CSAT3; 10 cm path length) recorded the three velocity components and virtual temperature at $z = 2$ m at 20 Hz from June 10- 24 (2018). The vertical array comprised five heights at $z = 0.0625, 0.125, 0.25, 0.5,$ and 1.0 m, each instrumented with one Nano-Scale Thermal Anemometry Probe (NSTAP; 60 µm sensing length) and one temperature variant (T-NSTAP; 200 µm). Both probes were operated in constant-current anemometry and sampled at 100 Hz. The hot- and cold-wire sensors were separated by approximately 3.6 cm (corresponding to 2.54 cm offsets in both the vertical and horizontal directions) at each height. The motivation for this configuration was to develop a low-cost circuitry using entirely off-the-shelf components enabled by the nanoscale sensors' inherently high resolution and small thermal mass. Details about the nanoscale sensors and their in-house operating circuits based on a Wheatstone bridge without additional feedback circuitry can be found elsewhere (K. Huang et al., 2021; K. Y. Huang & Katul, 2022). A secondary objective is to evaluate the probe's viability for atmospheric turbulence measurements near the ground, particularly its performance in resolving covariances. A three-day intensive operational period (18–20 June 2018) yielded nine 30-min records spanning slightly unstable (2), near-neutral (4), and slightly stable (3) conditions. Missing data in the subsequent analysis correspond to temperature sensor breakage at $z = 0.5$ m for all cases, and at $z = 0.0625$ m for the stable cases.

Figure 2. Left: The 1-m vertical array of nano-scale sensors at the SLTEST site. Right: The Duke Forest Grass Clearing site.

3.2 The Duke Forest Grass Clearing

The three velocity components and virtual temperature were measured using a triaxial sonic anemometer between July 12 and 16 (1995) at z=5.2 m above a grass surface within a forest clearing at the Blackwood division of the Duke Forest near Durham, North Carolina. The forest clearing dimensions were 480 m by 305 m and the mast was situated at 250 m and 160 m from the north-end and west-end portions of a 10 m Loblolly pine forest edge respectively. The sampling frequency and sampling duration per run were 56 Hz and 19.5 min. The sonic anemometer (Gill Instruments/1012R2) path length was 0.149 m. The 5-day experiment provided 128 runs spanning slightly stable to dynamic-convective conditions. The site, experimental setup, and data processing are described elsewhere (G. Katul et al., 1997) and not repeated here.

4 Results and Discussion

Findings from the RANS analysis are first presented followed by a discussion on the realizability constraints and estimates for R_h. Spectral and co-spectral outcomes are featured with a focus on the CSB model and its findings for inertial subrange and production scales. To convert time to wavenumbers, Taylor's frozen turbulence hypothesis (Taylor, 1938; Everard et al., 2021; Deshpande et al., 2023) is used without additional adjustments arising from finite turbulent intensities (J. Lumley, 1965; J. Wyngaard & Clifford, 1977; Hsieh & Katul, 1997).

4.1 Mean Longitudinal Heat Flux Profile

Ensemble-averaged profiles of the correlation coefficient $R_{u\theta} = \overline{u'\theta'_v}/(\sigma_u\sigma_\theta)$ for each stability class from the vertical array at SLTEST show finite values but weak dependence on height z (Fig. 3a). Corresponding ensemble-averaged profiles of $\overline{u'\theta'_v}$ are presented in Fig. 3b, along with fitted Eqs. 12 and 14 for the near-neutral and the unstable cases, respectively. These fitted equations are solutions to the RANS budget when the dominant balance is between flux transport and pressure decorrelation. A clear z-dependence in these measured profiles indicates a significant flux transport contribution. Although some vertical variation in $\overline{u'\theta'_v}$ appears under unstable conditions (mainly due to the $z = 2$m sonic anemometer measurements), the sonic anemometer measurements (open symbols) are likely underestimating the covariance and variances due to large anemometer path length with respect to the low measurement height ($z = 2$ m). For this reason, $R_{u\theta}$ from the sonic anemometer aligns better with the SLTEST measurements than $\overline{u'\theta'_v}$ since both numerator and denominator defining $R_{u\theta}$ are similarly under-estimated. The weak vertical variation in $R_{u\theta}$ therefore suggests that while flux transport may be finite near the ground, it appears to play only a minor role in the mean longitudinal heat flux budget, with the dominant balance between production and pressure decorrelation.

4.2 Thermal Stratification Effects on $R_{u\theta}$ and Its Realizability Constraint

Across the two sites, the $R_{u\theta}$ exhibit expected behavior across stability regimes (Fig. 4a), with $R_{u\theta} = 0$ at $\xi = 0$ and $R_{u\theta} \approx \pm 0.5$ for $|\xi| > 0.01$. The sign reversal across $\xi = 0$ reflects the transition between upward transport of heat in unstable conditions and downward transport in stable conditions. The constraint $R_{u\theta} \leq +0.64$ for near-neutral to slightly unstable conditions (based on literature values of $R_{w\theta} = 0.5$ and $R_{uw} = -0.35$) bounds $R_{u\theta}$ for $|\xi| < 0.05$. Moreover, all $|R_{u\theta}|$ values satisfy the realizability inequality (Eq. 19). Fig. 4b also shows the attained fraction of the upper bound

$$\rho = \frac{|R_{u\theta}|}{|R_{uw}R_{w\theta}| + \sqrt{1 + R_{uw}^2 R_{w\theta}^2 - (R_{uw}^2 + R_{w\theta}^2)}} \in [0, 1]. \tag{45}$$

A $\rho = 1$ corresponds to an equality limit against stability. It can be seen that the equality limit is never reached, but near-neutral and stable conditions seem to reach about 0.6, while this fraction decreases with instability.

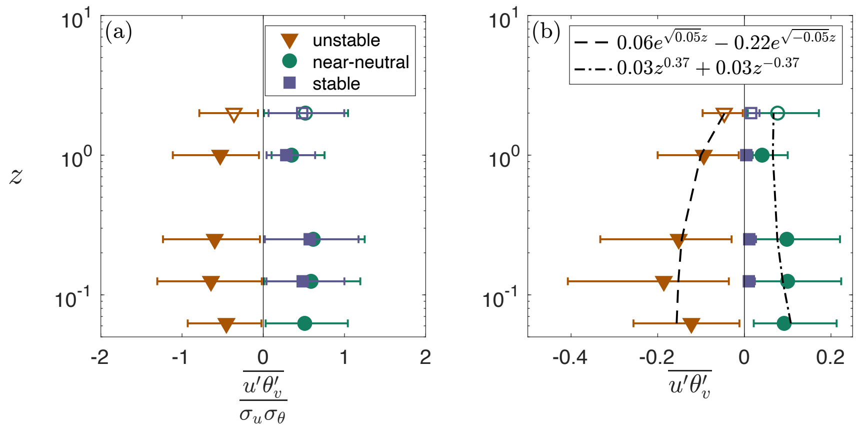

Figure 3. Profiles of $R_{u\theta} = \overline{u'\theta'_v}/(\sigma_u\sigma_\theta)$ (a) and of the longitudinal heat flux (b) at SLTEST from the vertical array (solid symbols) and from the sonic anemometer for $z = 2$ m (open symbols). Horizontal error bars denote across-run variability. For the longitudinal heat flux, fitted solutions of Eqs. 12 and 14 for the near-neutral and the unstable cases, respectively, are also shown. For the stable case, the exponent a_n is calculated based on measured $\phi_{TKE}(0)$ from the adjacent sonic anemometer.

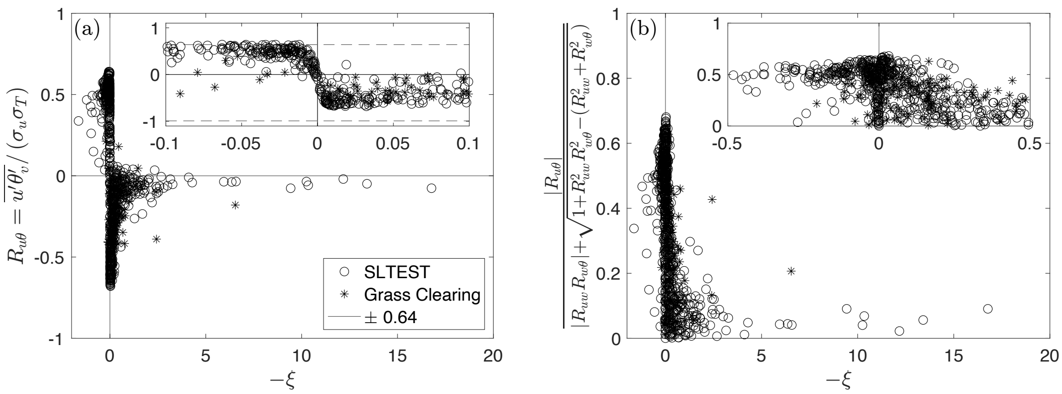

Figure 4. (a) Variations of the correlation coefficient $R_{u\theta}$ against stability for the SLTEST and the Duke Forest grass clearing datasets. Horizontal dashed lines represent the the realizability constraints $R_{u\theta} \in [-0.99, +0.64]$ based on values of $R_{w\theta} = 0.5$ and $R_{uw} = -0.35$. (b) Magnitudes of measured $R_{u\theta}$ normalized by the realizability constraint against stability.

4.3 Thermal Stratification Effects on R_h

As shown in Figure 5a, both sites confirm that $R_h \approx 3$ for near-neutral conditions, with R_h decreasing rapidly as instability increases but approaching ≈ 4 under near-neutral and slightly stable conditions. These values are consistent with those reported in the literature (Kader & Yaglom, 1990), lending confidence in the reliability of the present dataset despite differences in site and instruments. For $|\xi| < 0.05$ (near-neutral conditions), the small sensible heat flux leads to substantial scatter in R_h. Thus, Fig. 5b presents $\overline{u'\theta'_v}$ against $\overline{w'\theta'_v}$ for these conditions ($|\xi| < 0.05$) only. With calculated SLTEST values of $\phi_m(0) = 1.58$, $\phi_h(0) = 1.30$, $\phi_\varepsilon(0) = 1.00$ (from the vertical array at $z = 1$ m) and $\phi_{TKE}(0) = 5.93$ (from the sonic anemometer at $z = 2$ m), Equation 18 yields $R_h = 3.57$ in good agreement with measurements. The $R_h = 3$ value based on expected MOST

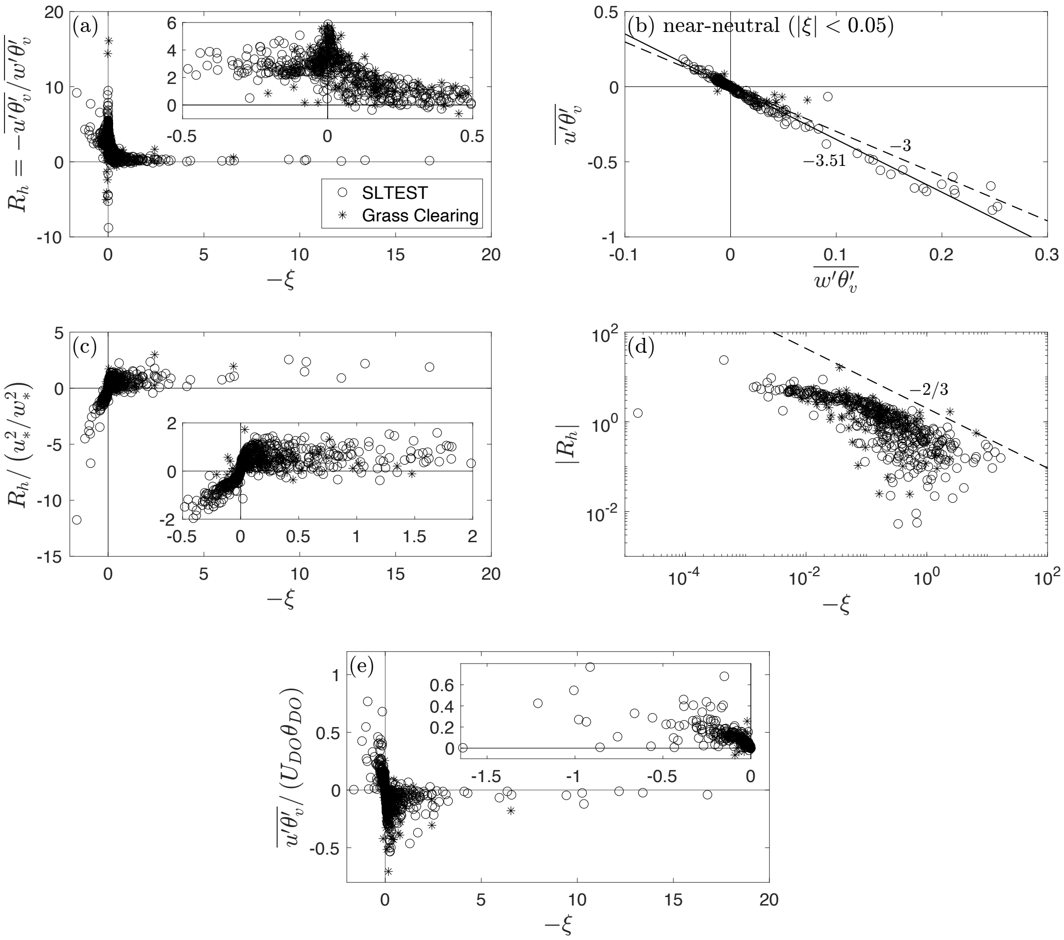

Figure 5. (a) Variations of R_h with the stability parameter ξ. (b) The relation between $\overline{u'\theta_v'}$ and $\overline{w'\theta_v'}$ for near-neutral conditions only set at $|\xi| < 0.05$. The dashed line is the prediction $R_h = 3$ based on expected MOST values from the literature. The solid line is the prediction $R_h = 3.85$ based on calculated $\phi_m = 1.58$, $\phi_h = 1.30$, $\phi_\varepsilon = 1.00$ from hot-wire data at $z = 1$ m and $\phi_{TKE} = 5.93$ from the sonic anemometer at the SLTEST site. (c) Variations of $R_h/(u_*^2/w_*^2)$ with the stability parameter ξ. DDA predicts $R_h/(u_*^2/w_*^2) \to constant$. (d) Variations of R_h with $-\xi$, with the dashed line representing the predicted DDA scaling of $R_h \sim \xi^{-2/3}$. (e) Variations of $\overline{u'\theta_v'}$ in Dougherty-Ozmidov scaling with stability for the SLTEST and the Duke Forest grass clearing sonic anemometer datasets. Although N_{BV} is undefined when $\Gamma_\theta < 0$, results for all stability conditions are shown for completeness since N_{BV} cancels out. Inset shows stable conditions ($-\xi < 0$), where the scaling is expected to be valid.

values at $\xi = 0$ ($\phi_m(0) = 1$, $Pr_t(0) = 1$, $\phi_\varepsilon(0) = 1$, and $\phi_{TKE}(0) = 6.7$) is also shown for reference.

Figure 5c shows R_h normalized by u_*^2/w_*^2 based on DDA scaling, which exhibits better collapse than MOST-based scaling, particularly in the near-neutral region. Consistent with DDA predictions for dynamically convective conditions, $R_h/(u_*^2/w_*^2)$ approaches an approximately constant value (≈ 0.5), despite some scatter, as $-\xi$ increases. The corresponding DDA prediction of $R_h \sim \xi^{-2/3}$ is shown in Fig. 5d, where a near $-2/3$ power-law scaling in $|R_h|$ emerges as $-\xi$ increases. Overall, the results suggest some cautionary support for DDA over MOST for the longitudinal heat flux scaling.

4.4 Dougherty-Ozmidov Scaling for Stably Stratified Flows

Normalization of $\overline{u'\theta_v'}$ with the Dougherty–Ozmidov scaling variables using both the SLTEST and the Duke Forest Grass clearing sonic datasets are shown in Fig. 5 (e). Although N_{BV} is undefined when $\Gamma_\theta < 0$, it cancels out in the scaling ($U_{DO}\theta_{DO} = \varepsilon/\beta$) and therefore does not enter the plotted normalization. For $\xi > 0.2$ where the Dougherty–Ozmidov scaling is expected to hold, $\overline{u'\theta_v'}/U_{DO}\theta_{DO}$ tends towards a value of approximately 0.2. However, the scatter is evident in the strongly stable regime, likely reflecting increased intermittency and the suppression of turbulence by buoyancy forces, which amplify the sensitivity of flux estimates to small-scale variability and noise.

4.5 Spectral and Co-spectral Models

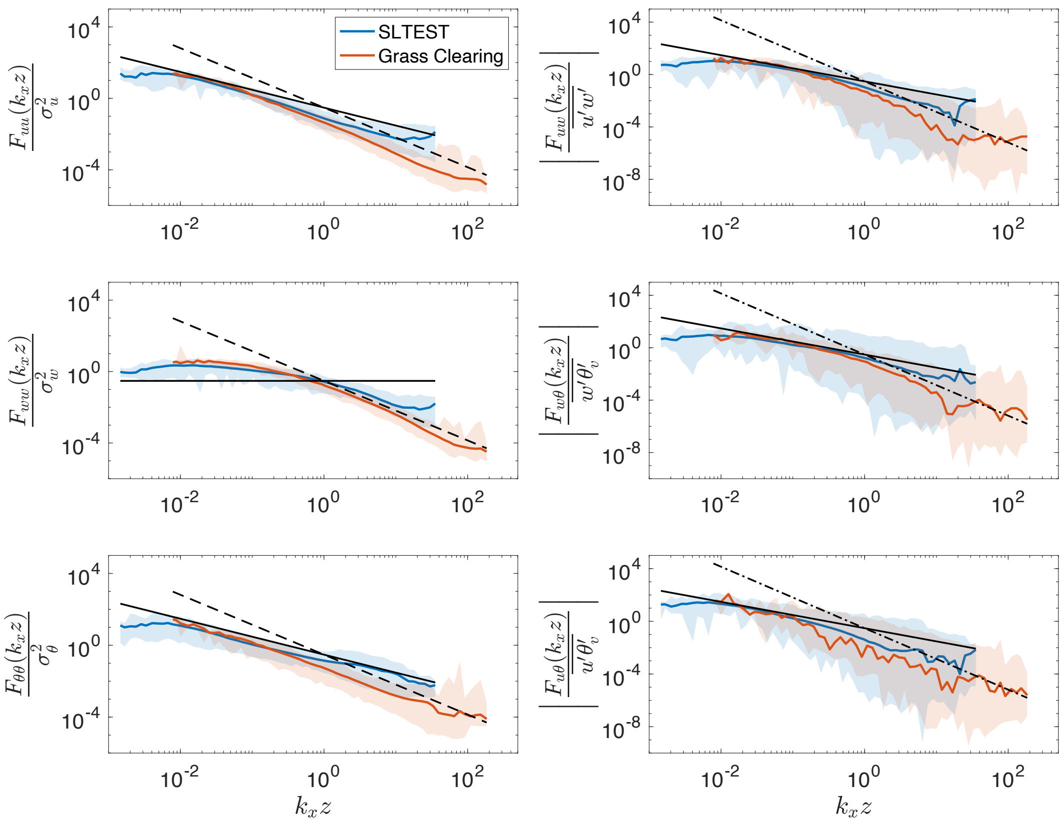

Figure 6. The dimensionless spectra (left) and co-spectra (right) for near-neutral conditions when the stability parameter $|\xi| < 0.05$. The wavenumber k_x is normalized by z. The scaling exponents $k_x^{-5/3}$ (dashed line) for the spectra and $k_x^{-7/3}$ (dash-dot line) for the co-spectra are also shown. Solid lines denote the expected k_x^{-1} scaling at large scales for all spectra and co-spectra, except for $F_{ww}(k_x)$, where the solid line indicates the expected k_x^0 scaling associated with wall-induced 'energy-splashing' at large scales.

Relevant spectra and co-spectra of the two velocity components (u' and w') and the virtual temperature (θ_v') from sonic anemometer data at both sites are shown in Figure 6 for near-neutral conditions ($|\xi| < 0.05$, consistent with the cases presented in Figure 5b). In the inertial subrange at the grass site ($z = 5.2$ m), the spectra exhibit the expected $k_x^{-5/3}$ slope for $k_x z > 2$, and the co-spectra $F_{uw}(k_x)$, $F_{wT}(k_x)$, and $F_{u\theta}(k_x)$ display an approximate $k_x^{-7/3}$ scaling. Although the SLTEST dataset exhibit a similar tendency toward the expected slopes, the inertial subrange behavior is less distinct, likely due to its proximity to the surface ($z = 2$ m). Spatial variability in surface heating at SLTEST– arising from the patchy distribution of salt deposits – may further contribute to the elevated noise observed in the co-spectra. At large scales (i.e. $k_x z < 0.5$), the spectra and co-spectra for both sites generally follow an approximate k_x^{-1} scaling, except for the vertical velocity spectra, which exhibits a k_x^0 region associated with energy splashing due to the randomizing effect of the ground on eddy impingement.

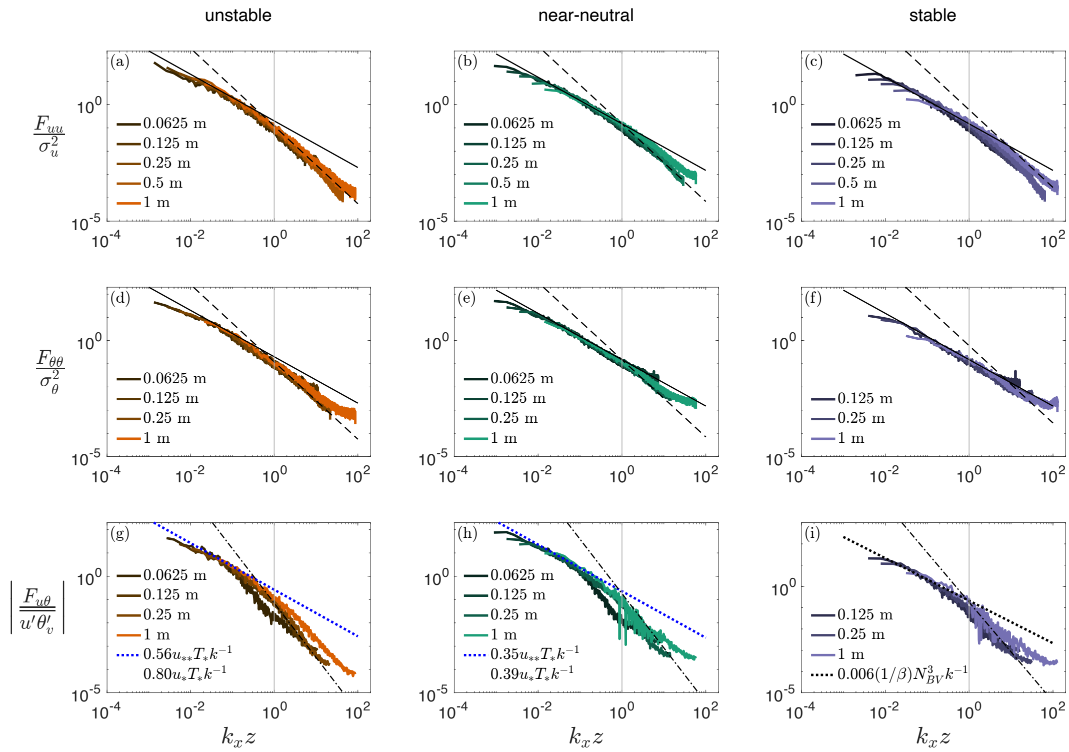

Figure 7. The dimensionless longitudinal velocity spectra (top row), temperature spectra (middle row), and co-spectra (bottom row) for unstable (left column), near-neutral (middle column), and stable (right column) conditions. The wavenumber k_x is normalized by z. The scaling exponents $k_x^{-5/3}$ (dashed line) for the spectra and $k_x^{-7/3}$ (dash-dot line) for the co-spectra are shown. The k_x^{-1} is also presented (solid line) for the spectra and co-spectra expected to hold for large scales.

Spectra and co-spectra of the horizontal velocity component (u') and virtual temperature (θ'_v) from the vertical array at SLTEST are shown for unstable, near-neutral, and stable conditions in Fig. 7. At large scales ($k_x z \in [1, 10]$), where the attached-eddy hypothesis is expected to hold, a k_x^{-1} scaling is evident across all stability regimes and for both the spectra and co-spectra. For the large scales of $F_{u\theta}$, both DDA and MOST normalization predict a k_x^{-1} dependence under near-neutral and unstable conditions, and the two frameworks yield comparable proportionality constants, as shown in Fig. 7(g) and (h). Under stable conditions, the Dougherty–Ozmidov scaling similarly predicts a k_x^{-1} dependence and is shown in Fig. 7(i).

For the inertial subrange, $F_{uu}(k_x)$ exhibits an approximate $k_x^{-5/3}$ scaling in all three stability cases. For $F_{\theta\theta}$, the $k_x^{-5/3}$ scaling is only apparent in the unstable condition. Under near-neutral and stable conditions, $F_{\theta\theta}$ exhibits limited inertial-subrange behavior and a more extended region of k_x^{-1} scaling. This finding is consistent with the enhanced logarithmic scaling of temperature variance (σ_θ) and higher-order moments discussed in K. Y. Huang et al. (2023). In the cospectra $F_{u\theta}(k_x)$, the inertial subrange behavior seems to be approaching $k_x^{-7/3}$ for all stability cases although the slopes are shallower. At the lowest measurement height, $F_{u\theta}(k_x)$ exhibits a faster decay and a distinct dip around $k_x z \approx 1$, most pronounced under near-neutral and unstable conditions. This behavior likely reflects reduced coherence between velocity and temperature fluctuations in the immediate vicinity of the surface– where shear production dominates and buoyancy-driven structures are disrupted – as well as effects from probe separation, since the relative sensor spacing becomes significant at the smallest z. Excluding the lowest measurement height, the slopes m (where $F_{u\theta} \sim k_x^{-m}$) over the range $1 \leq k_x z \leq 20$ are 2.10 ± 0.23, 1.85 ± 0.36, and 1.62 ± 0.28 for the unstable, near-neutral, and stable cases, respectively.

Cospectral data from the vertical array at SLTEST are first used to evaluate the constant scale-wise correlation hypothesis (Fig. 8). In contrast to Antonia and Zhu (1994), where a constant $F_{u\theta}/\left(F_{uu}F_{\theta\theta}\right)^{1/2} \approx 0.1$ was observed within the inertial subrange, no such constant correlation is evident in the present dataset. The correlation coefficients within the inertial subrange roll off at height-dependent rates and onset scales, with earlier transitions generally occurring closer to the surface, and remain approximately constant only at large scales. At very high wavenumbers, the correlations flatten again at a scale corresponding roughly to the distance between the u' and θ_v' probes ($k_x d \approx 1$; Fig. 8 bottom row), as the sensors become spatially separated relative to the smallest eddies. The fact that the breakpoint does not occur exactly at $k_x d = 1$ could reflect random sweeping effects, where large-scale motions advect and distort the small-scale eddies, leading to additional decorrelation beyond that expected from geometry alone. Similar results are observed from the sonic anemometer data at both the SLTEST and grass sites under near-neutral conditions (not shown).

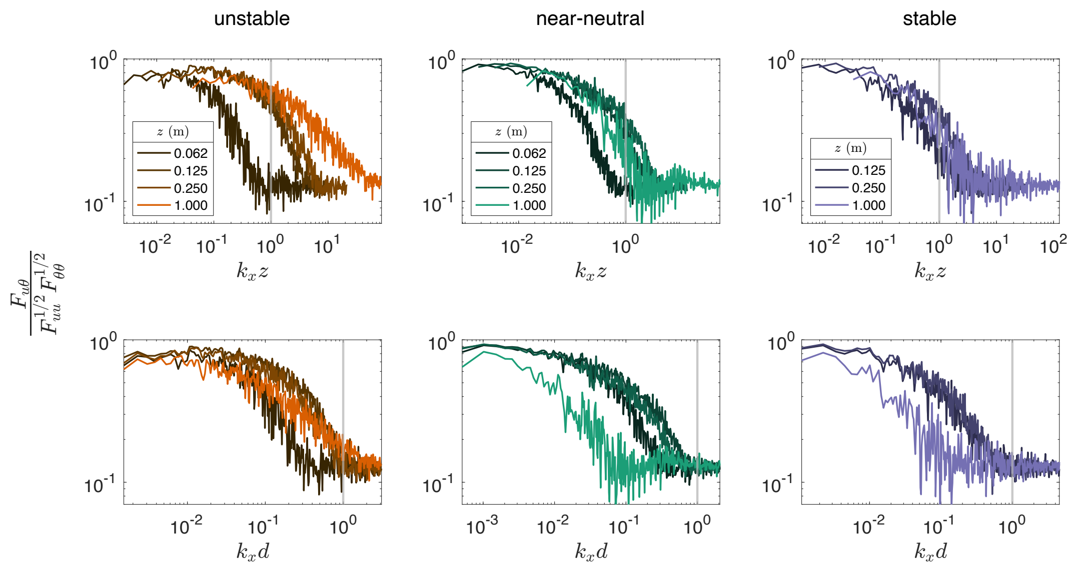

Figure 8. Top row: Scale-wise correlation $\rho(k_x)$ for slightly unstable (left), near-neutral (middle), and slightly stable (right) conditions at the SLTEST site. Bottom row: Same as top row but the wavenumber normalization is based on the separation distance between θ_v' and u' measurements instead of z to emphasize the scales experiencing loss of covariance due to instrument configuration.

4.6 The Co-Spectral Budget

Solutions to the co-spectral budget is examined using the SLTEST data. The production terms $|F_{wT}\Gamma|$ and $|F_{uw}\Gamma_\theta|$, as well as their sum, are first calculated and shown for unstable, near-neutral, and stable conditions in Fig. 9(a)-(c). The cospectra F_{wT} and F_{uw} are computed from the sonic anemometer measurements at $z = 2$ m, and the gradients Γ and Γ_θ from the vertical array and evaluated at $z = 1$ m. For both unstable and stable conditions, $|F_{uw}\Gamma_\theta|$ contributes more significantly to production, whereas under near-neutral conditions the two components are comparable at large scales, with $|F_{wT}\Gamma|$ becoming dominant in the inertial subrange. This partitioning is physically consistent as the relative importance of each term reflects the balance between shear and buoyancy production across stability regimes.

To capture observed power-laws in $P_{u\theta}(k_x)$, a model function in the spirit of the von Kármán spectrum is fitted to the production term beyond the spectral maximum,

$$P_{u\theta}(k_x) = \frac{A}{k_x}\frac{1}{(1 + Bk_x^2)^\gamma}, \tag{46}$$

where A, B, and γ are constants determined from nonlinear regression. This formulation is selected because it reproduces the observed k_x^{-1} behavior for large scales (as $k_x \to 0$) and is not designed to capture the very large scales beyond this range. At small scales (large k_x), $P_{u\theta} \to AB^{-\gamma}k_x^{-1-2\gamma}$ such that $\gamma = 2/3$ corresponds to a $k_x^{-7/3}$ scaling. Best-fits are obtained for the unstable, near-neutral, and stable cases and presented in Fig. 9(a-c). The near-neutral and unstable cases exhibit fitted exponents of $\gamma = 0.50$ and 0.59, corresponding to limiting high-wavenumber slopes of approximately k_x^{-2} and $k_x^{-2.18}$, respectively. In contrast, the stable case displays a steep decay with $\gamma = 1.29$ and $P_{u\theta} \sim k_x^{-3.56}$, indicating that covariance generation is confined almost entirely to the large eddies with minor contributions from the inertial subrange.

Figure 9(d)-(l) present the cospectra $|F_{u\theta}(k_x)|$ at $z = 0.125, 0.25$ and 1 m under unstable, near-neutral, and stable conditions. The fitted co-spectral general solutions are shown for large eddies ($1/10 < k_x z < 1$; Eq. 44 with $k_a = z$) and for the inertial subrange ($1 < k_x z < 20$; Eq. 42), with $A_p = A$, $\beta_p = 1$,$A'_p = AB^{-\gamma}$, and $\beta'_p = 1+2\gamma$ (determined from the large-k_x and small-k_x limits of the fitted model production). The homogeneous and particular (production-driven) components of the solutions are also shown to evaluate their relative importance across scales and stability regimes.

In the large-eddy range, the particular and homogeneous solutions are comparable at the lowest measurement height for all three stability regimes, indicating that both production and inertial transfer shape the cospectra. At the lowest height, where $1/z$ gradients are strongest and scale separation is limited, the production-driven contribution remains appreciable, yielding a composite spectrum as predicted by dimensional analysis. With increasing height, the particular contribution decays while the homogeneous term becomes dominant, implying that local production plays a progressively smaller role in setting the cospectral structure with increasing z. A similar pattern holds in the inertial subrange: at lower heights the particular and homogeneous contributions are still comparable, but the particular term diminishes with height (i.e., with increasing $|z/L|$), rendering production negligible.

Overall, across both the large-eddy and inertial-subrange scales, the homogeneous solution remains important throughout, whereas the particular solution (driven by the production term) is significant only very close to the surface, and its influence diminishes progressively with both increasing wavenumber and increasing stratification.

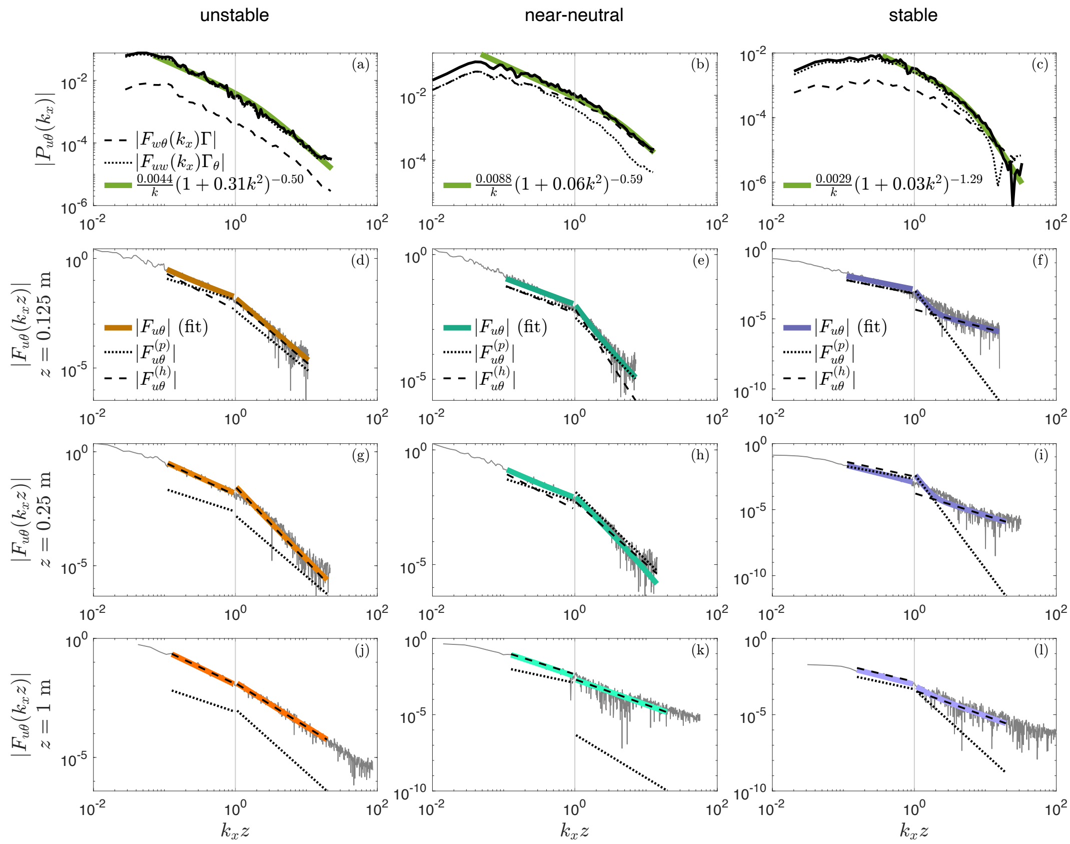

Figure 9. The two scale-wise production terms in the co-spectral budget and the regression fit to their sum when using Equation 46 for the unstable (a), near-neutral (b), and the stable (c) cases. Cospectra $|F_{u\theta}(k_x)|$ across height and stability (d) to (l), with each panel showing the fitted solutions for the large-eddies and inertial-subrange regimes, and their decomposed particular (production-driven) $|F^{(p)}_{u\theta}(k_x)|$ and homogeneous $|F^{(h)}_{u\theta}(k_x)|$ contributions.

5 Conclusions

This work examined the mean and spectral characteristics of the longitudinal turbulent heat flux through its Reynolds-averaged Navier-Stokes equations and its co-spectral budget. The scaling behaviors are evaluated using two experiments: (i) a nanoscale sensing platform within the first meter above the surface with a nearby sonic anemometer at $z = 2$ m over the Utah salt flats (SLTEST), and (ii) a conventional sonic anemometer deployed over a grass clearing in Duke Forest (North Carolina).

The Reynolds-averaged analysis showed that the vertical variation in the turbulent heat flux $\overline{u'\theta'_v}$ serves as a practical diagnostic for flux transport: when $\partial_z\overline{u'\theta'_v}$ is appreciable, the flux–transport term is non-negligible and comparable in magnitude to pressure–decorrelation; conversely, when $\overline{u'\theta'_v}$ shows little or no z-dependence, the flux–transport contribution is small and may be neglected. Accordingly, data at SLTEST showed that the profile of the longitudinal heat flux $\overline{u'\theta'_v}$ was nearly constant with height (no strong z-dependence), suggestion that the flux–transport contribution is small in a mean sense. Key nondimensional quantities including the correlation coefficient $R_{u\theta}$ and the ratio between horizontal and vertical heat flux R_h were consistent with values reported in the literature for surface-layer turbulence. The data also adhered to realizability constraints: under stable stratification $|R_{u\theta}|$ attained about 0.6 of its theoretical upper limit, and this fraction decreased as atmospheric stability conditions became unstable. Directional Dimensional Analysis (DDA) produced an improved collapse in R_h across stability regimes relative to Monin–Obukhov Similarity Theory (MOST), indicating that DDA captures additional directional and anisotropic effects relevant to near-surface turbulence. Both field sites, despite contrasting heterogeneity and measurement techniques, showed comparable trends and stability dependence, underscoring the robustness of the observed relations.

The cospectral analysis explored the scale-dependent behavior of the longitudinal turbulent heat flux. The assumption of constant scale-wise correlation held only for the largest eddies, with correlations decreasing systematically toward higher wavenumbers, in contrast to earlier findings by Antonia and Zhu (1994) that reported a constant correlation extending in the inertial subrange.

The cospectral budget analysis revealed that the scaling in $F_{u\theta}(k_x)$ is dependent on two non-universal parameters: $A_{u\theta}$ from the flux transfer contribution and β_p from the production contribution. The parameter β_p is in turn dependent on two co-spectra, F_{uw} and $F_{w\theta}$, that contribute to production. In the large eddies where the attached eddy hypothesis is expected to hold, a robust -1 scaling in $F_{u\theta}(k_x)$ emerges since both F_{uw} and $F_{w\theta}$ exhibit approximate k^{-1} behavior. That is, since the production term $P_{u\theta}(k_x) = F_{uw}(k_x)\Gamma_\theta + F_{w\theta}(k_x)\Gamma$ will likewise follow a k_x^{-1} dependence at the large scales, $F_{u\theta}(k_x)$ can inherit the same slope through the particular solution (β_p' in Eq. 44). The homogeneous solution, governed by the relative strength of the flux-transfer coefficient $A_{u\theta}$, either matches this -1 scaling when $A_{u\theta}$ is large or becomes subdominant when $A_{u\theta}$ is small. Consequently, $F_{u\theta}(k_x)$ tends to display an overall k_x^{-1} dependence at large scales, consistent with observations and dimensional arguments from DDA, MOST, and Dougherty-Ozmidov scaling.

Within the inertial subrange, however, $F_{u\theta}(k_x)$ exhibits a large variability of cospectral slopes. Just like in the large eddies, how $F_{u\theta}(k_x)$ scales can be traced through the cospectral budget analysis to β_p, the production term scaling that in turn depends on the F_{uw} and $F_{w\theta}$ scaling, and the flux-transfer coefficient $A_{u\theta}$. However, unlike in the large eddies where F_{uw} and $F_{w\theta}$ both scale as k_x^{-1}, they tend to exhibit anomalous scaling in the inertial subrange, thus contributing to the wide range of scaling exponents reported in the literature. This framework reconciles long-standing discrepancies in reported inertial subrange exponents by explicitly linking deviations from universality to non-conserved flux transfer mechanisms unique to the longitudinal heat flux.

Further, decomposition of the cospectral budget into particular and homogeneous components allowed examination of the relative roles of production and flux-transfer in the cospectral evolution. SLTEST data showed that while the flux transport term appears insignificant in the mean balance, the flux transfer term plays a non-negligible role in its spectral counterpart across all scales and stability conditions. The particular solution (driven by the production term) was comparable to the homogeneous solution only close to the surface and rapidly falls off as z increases. For all stability cases in the inertial subrange, $A_{u\theta} > 0.68$ and suggests that flux-transfer is an important mechanism in the scale-to-scale evolution of the $F_{u\theta}(k_x)$. These results and observations are consistent with dimensional analysis for the inertial subrange, with Γ and Γ_θ entering the production term (and thus the particular solution), and ε setting the eddy relaxation time and ε_θ the scalar cascade rate (and thus the homogeneous solution).

Overall, the findings establish that the longitudinal heat turbulent flux, though often neglected in closure schemes, provides a new perspective into scale-dependent energy exchange and anisotropy in stratified turbulence. By elucidating when and how flux-transfer terms modulate spectral slopes, the results offer a pathway for improved parameterization of non-local transport in atmospheric models.

From an experimental perspective, the obtained fluxes and spectral behaviors closely match those derived from conventional sonic anemometers, supporting the use of nano-scale sensors and simplified anemometer circuitry for low-cost, fine-scale atmospheric measurements - especially close to the ground. One limitation lies in the absence of vertical-velocity (w) measurements, which would enable fully co-located $\overline{w'\theta_v'}$ estimates and improved cospectral closure. Future developments toward two-dimensional nano-scale sensor systems are expected to enhance characterization of surface-layer flux dynamics and inform improved parameterizations of wall models for turbulent heat and momentum exchanges.

Conflict of Interest

The authors declare no conflicts of interest relevant to this study.

Open Research Section

The dataset is available at `https://github.com/atlas-uh/longitudinal_heat_flux` for the peer review process, and will be permanently archived and assigned a DOI through Zenodo upon acceptance.

Acknowledgments

GK acknowledges support from the U.S. National Science Foundation (NSF-AGS-2028633) and the U.S. Department of Energy (DE-SC0022072). The authors declare there are no conflicts of interest for this manuscript.

References

Antonia, R., & Zhu, Y. (1994). Inertial range behaviour of the longitudinal heat flux cospectrum. *Boundary-Layer Meteorology*, *70*, 429–434.

Besnard, D., Harlow, F., Rauenzahn, R., & Zemach, C. (1996). Spectral transport model for turbulence. *Theoretical and Computational Fluid Dynamics*, *8*(1), 1–35.

Betchov, R., & Yaglom, A. (1971). Notes on similitude theory for turbulence in an un-stably stratified fluid. *Izv. Akad. Nauk SSSR. Fizika Atmos. i Okeana*, *7*, 1270–1279.

Bink, N., & Meesters, A. (1997). Comment on 'estimation of surface heat and momentum fluxes using the flux-variance method above uniform and non-uniform terrain'by katul et al.(1995). *Boundary-Layer Meteorology*, *84*(3), 497–502.

Bos, W., Touil, H., Shao, L., & Bertogli, J. (2004). On the behavior of the velocity-scalar cross correlation spectrum in the inertial range. *Physics of Fluids*, *16*, 3818–3823.

Bos, W. J., & Bertoglio, J.-P. (2007). Inertial range scaling of scalar flux spectra in uniformly sheared turbulence. *Physics of Fluids*, *19*(2), 025104.

Bou-Zeid, E., Gao, X., Ansorge, C., & Katul, G. G. (2018). On the role of return to isotropy in wall-bounded turbulent flows with buoyancy. *Journal of Fluid Mechanics*, *856*, 61–78.

Brugger, P., Katul, G., De Roo, F., Kröniger, K., Rotenberg, E., Rohatyn, S., & Mauder, M. (2018). Scalewise invariant analysis of the anisotropic reynolds stress tensor for atmospheric surface layer and canopy sublayer turbulent flows. *Physical Review Fluids*, *3*(5), 054608.

Canuto, V., Minotti, F., Ronchi, C., Ypma, R., & Zeman, O. (1994). Second-order closure pbl model with new third-order moments: Comparison with LES data. *Journal of Atmospheric Sciences*, *51*(12), 1605–1618.

Caughey, S. (1977). Boundary-layer turbulence spectra in stable conditions. *Boundary-Layer Meteorology*, *11*(1), 3–14.
Caughey, S., Wyngaard, J., & Kaimal, J. (1979). Turbulence in the evolving stable boundary layer. *Journal of Atmospheric Sciences*, *36*(6), 1041–1052.
Cava, D., & Katul, G. (2012). On the scaling laws of the velocity-scalar cospectra in the canopy sublayer above tall forests. *Boundary-Layer Meteorology*, *145*, 351–367.
Charuchittipan, D., & Wilson, J. (2009). Turbulent kinetic energy dissipation in the surface layer. *Boundary-Layer Meteorology*, *132*(2), 193–204.
Choi, K.-S., & Lumley, J. L. (2001). The return to isotropy of homogeneous turbulence. *Journal of Fluid Mechanics*, *436*, 59–84.
Deshpande, R., de Silva, C. M., & Marusic, I. (2023). Evidence that superstructures comprise self-similar coherent motions in high Reynolds number boundary layers. *Journal of Fluid Mechanics*, *969*, A10.
Dougherty, J. (1961). The anisotropy of turbulence at the meteor level. *Journal of Atmospheric and Terrestrial Physics*, *21*(2-3), 210–213.
Durbin, P. (1993). A Reynolds stress model for near-wall turbulence. *Journal of Fluid Mechanics*, *249*, 465–498.
Everard, K., Katul, G., Lawrence, G., Christen, A., & Parlange, M. (2021). Sweeping effects modify Taylor's frozen turbulence hypothesis for scalars in the roughness sublayer. *Geophysical Research Letters*, *48*(22), e2021GL093746.
Garratt, J. (1992). *The atmospheric boundary layer.* Cambridge University Press, Cambridge, Great Britain.
Grachev, A. A., Andreas, E. L., Fairall, C. W., Guest, P. S., & Persson, P. O. G. (2015). Similarity theory based on the Dougherty–Ozmidov length scale. *Quarterly Journal of the Royal Meteorological Society*, *141*(690), 1845–1856.
Guo, H., Golaz, J.-C., Donner, L., Wyman, B., Zhao, M., & Ginoux, P. (2015). CLUBB as a unified cloud parameterization: Opportunities and challenges. *Geophysical Research Letters*, *42*(11), 4540–4547.
Hanjalić, K., & Launder, B. (2021). Reassessment of modeling turbulence via Reynolds averaging: A review of second-moment transport strategy. *Physics of Fluids*, *33*(9), 091302.
Hsieh, C.-I., & Katul, G. G. (1997). Dissipation methods, Taylor's hypothesis, and stability correction functions in the atmospheric surface layer. *Journal of Geophysical Research: Atmospheres*, *102*(D14), 16391–16405.
Huang, K., Brunner, C., Fu, M., Kokmanian, K., Morrison, T., Perelet, A., ... Hultmark, M. (2021). Investigation of the atmospheric surface layer using a novel high-resolution sensor array. *Experiments in Fluids*, *62*(4), 76.
Huang, K. Y., Fu, M. K., Byers, C. P., Bragg, A. D., & Katul, G. G. (2023). Logarithmic scaling of higher-order temperature moments in the atmospheric surface layer. *International Journal of Heat and Fluid Flow*, *102*, 109162.
Huang, K. Y., & Katul, G. G. (2022). Profiles of high-order moments of longitudinal velocity explained by the random sweeping decorrelation hypothesis. *Physical Review Fluids*, *7*(4), 044603.
Kader, B., & Yaglom, A. (1990). Mean fields and fluctuation moments in unstably stratified turbulent boundary layers. *Journal of Fluid Mechanics*, *212*, 637–662.
Kader, B., & Yaglom, A. (1991). Spectra and correlation functions of surface layer atmospheric turbulence in unstable thermal stratification. In *Turbulence and coherent structures* (pp. 387–412). Springer.
Kader, B., Yaglom, A., & Zubkovskii, S. (1989). Spatial correlation functions of surface-layer atmospheric turbulence in neutral stratification. *Boundary-Layer Meteorology*, *47*(1), 233–249.
Kaimal, J., & Finnigan, J. J. (1994). *Atmospheric boundary layer flows: Their structure and measurement.* Oxford University Press.

Kaimal, J., Wyngaard, J., Izumi, Y., & Coté, O. (1972). Spectral characteristics of surface-layer turbulence. *Quarterly Journal of the Royal Meteorological Society*, *98*(417), 563–589.

Katul, G., & Hsieh, C.-I. (1997). Reply to the comment by bink and meesters. *Boundary-Layer Meteorology*, *84*(3), 503–509.

Katul, G., Hsieh, C.-I., & Sigmon, J. (1997). Energy-inertial scale interactions for velocity and temperature in the unstable atmospheric surface layer. *Boundary-Layer Meteorology*, *82*(1), 49–80.

Katul, G., Li, D., Chamecki, M., & Bou-Zeid, E. (2013). Mean scalar concentration profile in a sheared and thermally stratified atmospheric surface layer. *Physical Review E*, *87*.

Katul, G. G., Chu, C. R., Parlange, M. B., Albertson, J. D., & Ortenburger, T. A. (1995). Low-wavenumber spectral characteristics of velocity and temperature in the atmospheric surface layer. *Journal of Geophysical Research: Atmospheres*, *100*(D7), 14243–14255.

Katul, G. G., Porporato, A., Manes, C., & Meneveau, C. (2013). Co-spectrum and mean velocity in turbulent boundary layers. *Physics of Fluids*, *25*(9), 091702.

Katul, G. G., Porporato, A., Shah, S., & Bou-Zeid, E. (2014). Two phenomenological constants explain similarity laws in stably stratified turbulence. *Physical Review E*, *89*(2), 023007.

Kays, W. M. (1994). Turbulent Prandtl number. where are we? *ASME Journal of Heat Transfer*, *116*(2), 284–295.

Large, W. G., McWilliams, J. C., & Doney, S. C. (1994). Oceanic vertical mixing: A review and a model with a nonlocal boundary layer parameterization. *Reviews of Geophysics*, *32*(4), 363–403.

Launder, B., Reece, G., & Rodi, W. (1975). Progress in the development of a Reynolds-stress turbulence closure. *Journal of Fluid Mechanics*, *68*, 537–566.

Li, D. (2019). Turbulent prandtl number in the atmospheric boundary layer-where are we now? *Atmospheric Research*, *216*, 86–105.

Li, D., Salesky, S. T., & Banerjee, T. (2016). Connections between the ozmidov scale and mean velocity profile in stably stratified atmospheric surface layers. *Journal of Fluid Mechanics*, *797*, R3.

Lumley, J. (1965). Interpretation of time spectra measured in high-intensity shear flows. *Physics of Fluids*, *8*(6), 1056–1062.

Lumley, J. (1967). Similarity and the turbulent energy spectrum. *Physics of Fluids*, *10*, 855–858.

Lumley, J. L. (1979). Computational modeling of turbulent flows. *Advances in Applied Mechanics*, *18*, 123–176.

Mellor, G. L., & Yamada, T. (1982). Development of a turbulence closure model for geophysical fluid problems. *Reviews of Geophysics*, *20*(4), 851–875.

Monin, A. S., & Obukhov, A. M. (1954). Basic laws of turbulent mixing in the surface layer of the atmosphere. *Contrib. Geophys. Inst. Acad. Sci. USSR*, *151*(163), e187.

Mortarini, L., Katul, G., Mauricio Cely-Toro, I., Quaresma Dias-Júnior, C., & Mammarella, I. (2025). The role of thermal stratification on the co-spectral properties of momentum transport above an amazonian forest. *Quarterly Journal of the Royal Meteorological Society*, e5024.

Panofsky, H., & Mares, E. (1968). Recent measurements of cospectra for heat-flux and stress. *Quarterly Journal of the Royal Meteorological Society*, *94*(402), 581–585.

Pope, S. (2000). *Turbulent flows.* Cambridge, UK: Cambridge University Press.

Priestley, M. B. (1988). *The spectral analysis of time series.* Oxford University Press.

Stiperski, I., Katul, G. G., & Calaf, M. (2021). Universal return to isotropy of inhomogeneous atmospheric boundary layer turbulence. *Physical Review Letters*, *126*(19), 194501.

Taylor, G. I. (1938). The spectrum of turbulence. *Proceedings of the Royal Society of London. Series A-Mathematical and Physical Sciences*, *164*(919), 476–490.

Tennekes, H., & Lumley, J. (1972). *A first course in turbulence.* Cambridge, MA: MIT Press.

Wyngaard, J., & Clifford, S. (1977). Taylor's hypothesis and high–frequency turbulence spectra. *Journal of Atmospheric Sciences*, *34*(6), 922–929.

Wyngaard, J., & Coté, O. (1972). Cospectral similarity in the atmospheric surface layer. *Quarterly Journal of the Royal Meteorological Society*, *98*(417), 590–603.

Wyngaard, J. C. (2010). *Turbulence in the atmosphere.* Cambridge University Press.

Zeman, O., & Lumley, J. L. (1976). Modeling buoyancy driven mixed layers. *Journal of Atmospheric Sciences*, *33*(10), 1974–1988.

Zilitinkevich, S. (1973). Shear convection. *Boundary-Layer Meteorology*, *3*(4), 416–423.

Zilitinkevich, S., Gryanik, V. M., Lykossov, V., & Mironov, D. (1999). Third-order transport and nonlocal turbulence closures for convective boundary layers. *Journal of the Atmospheric Sciences*, *56*(19), 3463–3477.